AI & MRI: improved mapping of oxygenation in brain tumours

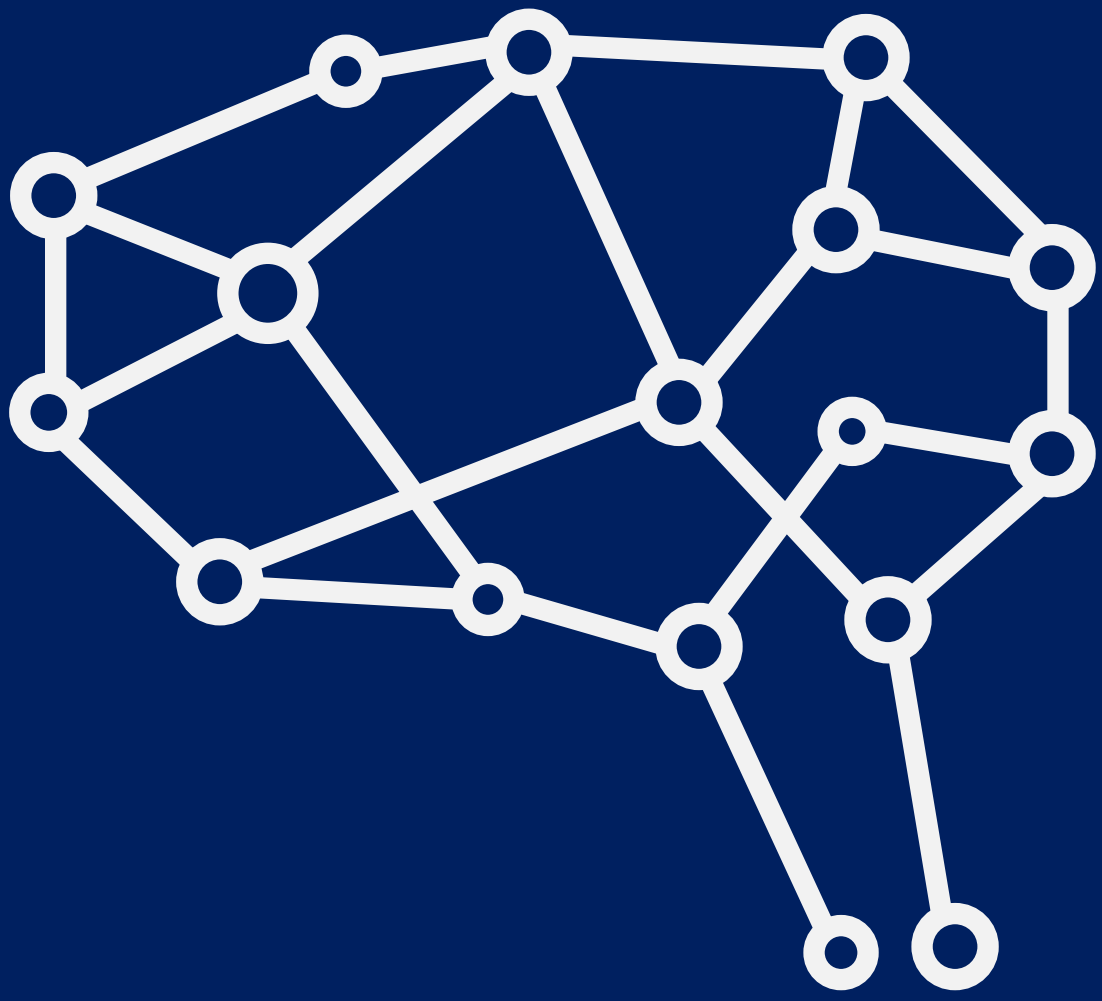

Mathijs Rosbergen

Technical Medicine – Imaging & Intervention

22-09-2021

TU Delft

Erasmus MC
University Medical Center Rotterdam

AI & MRI: improved mapping of oxygenation in brain tumours

by

Mathijs Rosbergen

22-09-2021

General information

Master program:	*Technical Medicine*
Track:	*Imaging & Intervention*
Student number:	*4480236*
Project duration:	*January 2021 – September 2021*

Supervisors

Technical supervisor:	*Dr. ir. Esther Warnert*
Medical supervisor:	*Prof. Dr. Marion Smits*
Additional supervisor:	*Fatemehsadat Arzanforoosh*
Additional supervisor:	*Sebastian van der Voort*

Thesis comittee members

Prof. Dr. Marion Smits (chair)	*Erasmus MC, Department of Radiology and Nuclear Medicine*
Dr. ir. Esther Warnert	*Erasmus MC, Department of Radiology and Nuclear Medicine*
Dr. Martijn Tannemaat	*LUMC, Department of Clinical Neurophysiology*

TU Delft

Erasmus MC
University Medical Center Rotterdam

Summary

Introduction Gliomas are the most common primary malignant brain tumours with a very poor survival. Resistance to chemotherapy and radiotherapy often occurs in these tumours due to hypoxia, which can be caused by different oxygenation parameters. Multiple magnetic resonance imaging (MRI) techniques are able to assess these oxygenation parameters. Since multiple artificial intelligence (AI) approaches exist to fuse these oxygenation images together, the goal of this research is to find and implement an AI approach to generate a combined representation of multiple oxygenation parameters acquired by MRI so hypoxia within brain tumours can be detected and located.

Literature study Multiple MR imaging techniques that are able to measure different oxygenation parameters have been reviewed in the literature study. In addition, an overview was given of different AI approaches for combining the acquired information of the discussed MR imaging techniques. Based on the literature findings, hierarchical clustering was the most promising AI approach for this research purpose.

Methods A specific MR imaging protocol was designed to assess information regarding tumour oxygenation within patients with brain tumours. After registration of the acquired images to the same space, the voxels of healthy brain tissues in these images were used for performing hierarchical clustering multiple times to identify the optimal parameter settings of the algorithm. Then the clustering was performed multiple times with different data types in order to achieve a decrease of required computational power. After segmentation of the tumour area in the MR images, the clustering was applied to the tumour voxels to generate a spatial map of the tumour showing the location of the clusters representing different states of oxygenation. Evaluation of the clusters was performed by visualizing the distribution of the oxygenation parameter values within the different clusters.

Results Three patients were included and underwent MR imaging. Results showed that ward linkage and Euclidean distance resulted in the highest clustering performance when performing hierarchical clustering on data of healthy brain tissue. Changing the data type of input data did not lead to a decrease in required computational power. Applying the hierarchical clustering with the optimal parameter settings on tumour voxels resulted in spatial maps of the different clusters within the tumour. Evaluation of the distribution of the oxygenation parameter values showed differences among different clusters within the patients. However, within two patients the number of clusters present within the tumour, changed when including different MR images in the clustering analysis.

Conclusion This research showed that hierarchical clustering is an AI approach which is able to identify clusters with a different distribution of oxygenation parameter values acquired by MR imaging. Visualizing these different clusters in a spatial map results in a combined representation of these oxygenation parameters. Despite the promising results, future work is needed to investigate other clustering methods regarding this research purpose, the importance of each individual MR technique, and a validation method of what type of oxygenation the clusters represent

Table of contents

Chapter 1
Introduction

Chapter 1 Introduction

1.1 Gliomas

Prevalence

Representing 75% of all malignant primary brain tumours, gliomas are the most common primary malignant brain tumours in adults.[1] These type of brain tumours that arise from glial or precursor cells, can occur anywhere in the central nervous system (CNS).[2] However, gliomas are mainly present in the frontal, temporal, parietal, and occipital lobe with a percentage of 23.6%, 17.4%, 10.6% and 2.8% respectively.[1, 3] Depending on the location of the tumour severe symptoms can occur, including a change in personality.[2, 4]

WHO classification

Besides glioblastomas there are many other subtypes of gliomas. In 2016 the World Health Organization (WHO) published their fourth version the WHO Classification of CNS tumours.[5] According to these guidelines, differentiating between the different subtypes of gliomas requires histologic and molecular information of the tumour which can be obtained by using brain imaging to perform brain biopsies. These outcomes are essential to determine the appropriate treatment.[6]

Survival

Besides these impactful symptoms, the survival among primary CNS tumours is very poor. Even though these tumours represent only 2% of all primary tumours, they account for 7% of all cancer-related deaths for patients under 70 years.[7] Prognostic factors which result in better outcomes are a younger age and better performance status of the patient with glioma.[3, 8, 9] However, survival among patients with gliomas still varies widely depending on the classification and grading of the tumour. Despite this variation, the overall survival rate is still very poor. This is evident in the case of patients with grade IV gliomas, also known as glioblastomas, with a 5-year survival rate of less than 5%.[8-11] In addition, solely glioblastomas represent already 45% of all malignant primary CNS tumours.[9]

Hypoxia

In gliomas, hypoxia is often present. This lack of oxygen leads, directly or indirectly, to resistance to chemotherapy and radiotherapy.[12, 13] A classic example of a direct effect on treatment is the absence of the physiochemical principle known as the oxygen enhancing effect. In this process, irradiating the tumour causes severe irreparable damage to the DNA strands due the presence of oxygen.[14] An indirect effect of hypoxia is changing the behaviour of tumour cells by activating transcription factors such as hypoxia induced factor 1 (HIF-1) resulting in a decreased chemo- and radiosensitivity of the tumour.[15] Determining whether and where a brain tumour contains hypoxia may allow for improved treatment planning. The absence of the oxygen enhancing effect, for example, could be compensated in radiotherapy by increasing the dose using the oxygen enhancing ratio.[16] Furthermore, assessing brain and tumour oxygenation can predict outcomes of patients with brain tumours undergoing therapy.[17] Spence et al. for instance showed that the volume and intensity of hypoxia in glioblastoma is predictive for a poor survival and time to progression after radiotherapy.[18] Therefore, brain and tumour oxygenation are important biomarkers in treatment planning and predicting outcomes of patients with gliomas undergoing treatment. This demonstrates that improvement of hypoxia imaging will result in a more personalized treatment of patients with gliomas.

1.2 Magnetic Resonance Imaging (MRI)

Basic principles of magnetic resonance imaging

To assess cerebral oxygenation and visualize the anatomy of the brain and tumour, multiple magnetic resonance imaging (MRI) techniques are available. MRI is an imaging technique that generates three-dimensional images by using the magnetic properties of protons, which are abundant in the human body. Each proton, or hydrogen nucleus, spins along an axis with a magnetic north-pole and south-pole, like the planet earth. The axes around which the protons spin are oriented in random directions. MRI uses a strong magnetic field to align the spin of these protons with the applied magnetic field. When a radiofrequency pulse is introduced, the protons are deflected out of alignment with the magnetic field. If the radiofrequency pulse is turned off, the protons return to their resting state and align again with the magnetic field. This causes the protons to emit energy in the form of a radio wave which is detected by receiver coils of the MR scanner. These signals are used to construct MR images of the body. A brief overview of this imaging process is shown in *Figure 1* .

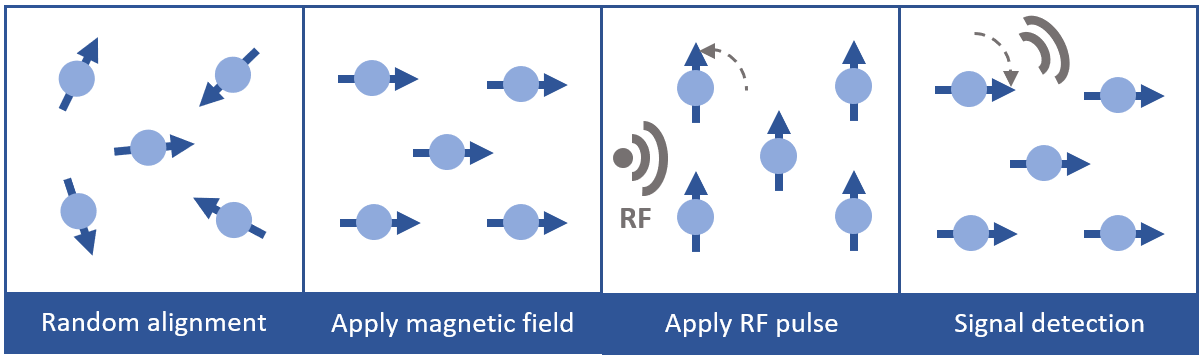

Figure 1: a simplistic overview of how protons are used for measuring a MRI signal.

MR imaging of brain anatomy and cerebral oxygenation

MRI can be divided into conventional imaging and advanced imaging. Conventional MRI refers to MR imaging in which mainly structural information rather than physiological information is acquired, while advanced MRI can be used to assess physiological and functional parameters of tissues. Both conventional and advanced MR imaging can be performed by T1-weighted and T2-weighted MR imaging. Within these techniques, the time taken for protons to return to their resting state is measured by two different methods. T1 relaxation time is defined as the time taken by the protons to return to their original longitudinal magnetization, while T2 relaxation time is defined as the time taken by protons to return the axial spin to their original state. The relaxation time of protons depends on the type of tissue where they are in and therefore resulting in different signal intensities shown in the generated MR image. Since the magnetic field is not homogeneous, T2* can also be measured with gradient-echo (GRE) sequences. T2* refers to the true T2 relaxation in combination with relaxation due to the magnetic field inhomogeneities and can be used to assess physiological information.[19] T2' is another parameters that can be measured and used for assessing further physiological information.[20] In addition, an exogenous contrast agent can be injected in the human body to add extra contrast into the image and may show enhancing areas of brain tumours.

To visualize different parameters of brain oxygenation, multiple MRI techniques have been developed, including: (i) arterial spin labelling (ASL) MRI to obtain cerebral blood flow (CBF)[21], (ii) streamlined quantitative blood oxygen level-dependent (sqBOLD) MRI to obtain oxygen extraction fraction (OEF)[22], and (iii) Dynamic Susceptibility Contrast (DSC) MRI to obtain vessel size measurements[23]. A comprehensive explanation of these techniques can be found in *Chapter 2 Literature Study*.

1.3 Artificial Intelligence

Machine learning

To understand how artificial intelligence (AI) can improve medical image processing, basic knowledge of AI and its subgroups is essential. AI refers to computer systems that can carry out tasks autonomously. For example, an AI algorithm can be trained to play chess. An important subfield of AI is machine learning, which refers to algorithms with the ability to make a prediction based on data given as input to the algorithm. Two large subfields of machine learning are supervised and unsupervised learning. An overview of AI and its subfields are shown in *Figure 2*.

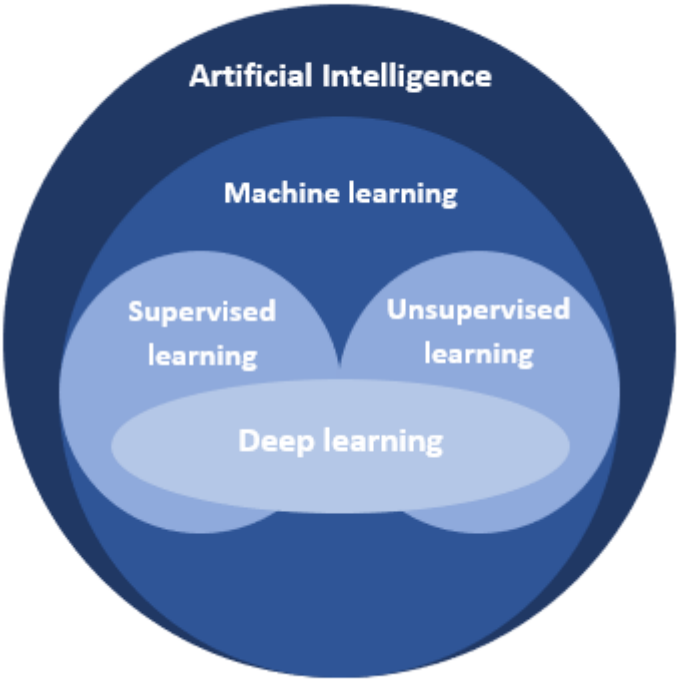

Figure 2: an overview of the different subfield of artificial intelligence.

Supervised learning

Supervised learning refers to AI models that make predictions based on labelled input data and make corrections based on a calculated loss between the predicted outcome and the label. To train an AI model through supervised learning to achieve a certain output, the model needs to know if its output is correct. For example, if an AI model is trained through supervised learning to recognize brain tumours in MR images, it needs to know if its prediction is correct. This is done by calculating the loss between the prediction of the model based on the input data and the labelled data. When the predicted output of the model is not correct, it needs to adjust its model parameters resulting in an

improved performance. The model adjusting its model parameters based on a certain output metric is called optimization. This process is visualized in *Figure 3*.

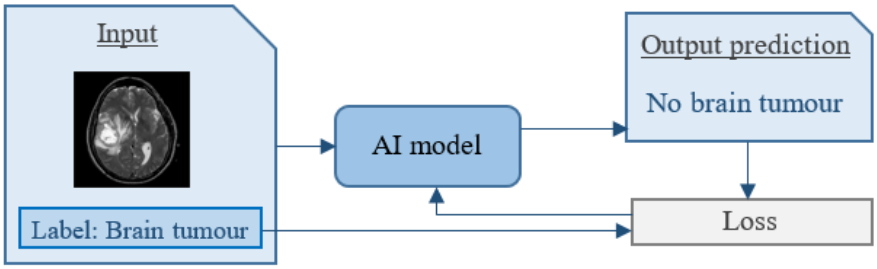

Figure 3: Outline of the supervised learning process. Input data is presented to the AI model. In this example the model is trained to recognize brain tumours in MR images. Based on the input data the AI model makes a prediction. When the prediction is incorrect, the loss between the label and the prediction will cause the model to change its model parameters to achieve the best performance.

Unsupervised learning

In contrast to supervised learning, unsupervised learning refers to AI models that discover patterns and information that was previously unknown without the need of human intervention. Some well-known methods of unsupervised learning are clustering and anomaly detection, in which data is clustered into groups with similar features and rare anomalies in data can be found respectively. The difference between supervised and unsupervised learning is shown in *Figure 4*.

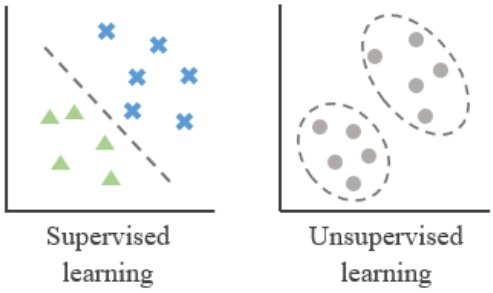

Figure 4: The difference between supervised and unsupervised learning. In this example, supervised learning uses labelled data to train an AI model so it can predict if new data points belong to the blue crosses or to the green triangles. In the example on the right, unsupervised learning is used to identify clusters (dashed lines) based on similar features of the data (grey dots) within the clusters.

Artificial neural networks

Artificial neural networks (ANNs) are one of the most recent approaches in the analysis of medical imaging.[24, 25] This AI method is a form of deep learning, which is a subfield of machine learning. ANN's work according to the same principle as the human brain, hence the name neural network. These networks use different neurons in its layers to process the data. The architecture consists of an input layer, one or more hidden layers and an output layer. After data is given as input to the input layer, feature extraction and transformations are performed in the hidden layers resulting in a certain output in the output layer. This network is trained by adjusting its model parameters during the training process. A specific ANN that can be applied for image processing is a convolutional

neural network (CNN). This type of ANN uses convolutional layers as hidden layers to process the input data.

1.4 Goals and objectives

Detecting and locating hypoxia and different oxygenation states within gliomas and brain tumours could improve treatment planning and potentially their poor treatment outcomes. However, hypoxia imaging can be difficult because multiple parameters play a role in the oxygenation status of brain tissue, which may alter in various manners to cause hypoxia. For example, hypoxia can occur due to a reduced CBF, but also due to a reduced diffusion of the oxygen out of the capillaries to the brain tissue. Multiple MRI techniques are capable of measuring these different parameters of brain oxygenation. However, a combined representation of these oxygenation parameters have not been extensively researched yet. Despite not widely explored yet, Stadlbauer's research[26] used multiple images acquired by different MRI techniques to assess and locate different metabolic states within brain tumours. The research presented in this study has a similar goal and focusses on finding and implementing an AI approach to create a combined representation of multiple oxygenation parameters acquired by MRI so hypoxia within brain tumours can be detected and located.

Chapter 2
Literature study

Chapter 2 Literature study

2.1 Introduction

Despite the ability to visualize different oxygenation parameters, there is no non-invasive method available to visualize oxygenation directly. In addition, a combined representation of the different oxygenation parameters has not been widely explored. However, Stadlbauer et al. performed tumour environment mapping resulting in a combined representation of different oxygenation status within gliomas. This new map was based on predefined threshold values of different oxygenation parameters acquired by multi-parametric MRI.[26] The application of artificial intelligence (AI) has the potential to make a useful contribution in this regard.[27] This is demonstrated by several studies which used AI to successfully apply multimodal MR image synthesis[28, 29], grade gliomas[30], and predict their IDH1 mutation status[31]. Therefore, AI is a promising method to combine different oxygen parameters and retrieve new features and information of existing MR imaging methods. This chapter contains a literature review that aims to give an overview of different MRI methods to assess brain oxygenation and different AI approaches to fuse these MR images into a complete brain oxygenation map.

2.3 Brain oxygenation: image acquisition

Arterial Spin Labelling

ASL is a recent and non-invasive MRI technique for quantifying CBF, which is slowly finding its way to widespread clinical adoption. This technique uses the ability of MRI to magnetically label arterial blood. First, a control image is required to acquire. Second, arterial blood in the feeding arteries of the brain is magnetically labelled by an inversion pulse. While this labelled blood flows to the brain capillaries as an endogenous tracer, the magnetization can be followed as it is transferred to brain tissue by capillary exchange. The exchange rate of these magnetically labelled protons to brain tissue is dependent on the perfusion of the tissue. Therefore, ASL is able to quantify perfusion. Third, subtracting the control image results in a perfusion weighted image. At last, a quantitative image representing CBF can be derived from the perfusion-weighted image by using a reference image, together with a kinetic model.[32-34]

In contrast to the current clinical standard assessment of perfusion with dynamic susceptibility contrast (DSC) imaging, an advantage of ASL is that there is no need for injecting an exogenous contrast agent. Research has shown a positive linear correlation between regional CBF assessment by ASL and DSC, for which a gadolinium-based contrast agent is required as tracer.[32] However, according to Warnert et al. IDH mutation within non-enhancing gliomas potentially affects this correlation, indicating care should be taken when assessing CBF with ASL in non-enhancing gliomas.[35]

However, ASL has multiple limitations which need to be taken into account when using its CBF maps for further processing. For example, ASL has an a poor signal-to-noise ratio (SNR). This is caused by a relatively low signal of the labelled blood (0.5% - 1.5%) compared to the full tissue signal. Besides, ASL has a low temporal resolution due to the period between the control image and labelled image as enough time needs to be allowed for the contrast to move from the labelling plane to the imaging plane.[36]

Transit time of the labelled blood, from the location where the label is generated to the region of interest for CBF measurement, is an important factor which can generate errors in quantifying CBF with ASL. Arterial transit time (ATT) refers to the period in which magnetically labelled blood reaches the imaging plane after it has been generated.[37] Intensity of ASL signals can vary due to variations in ATT caused by varying vessel sizes, lengths and tortuosity, even when the blood flow is the same in these vessels.[38] Therefore, multi post-labelling delay (PLD) ASL has been introduced that allows for fitting a full kinetic model to simultaneously assess ATT and CBF, reducing erroneous estimations of CBF due to transit time artefacts.[37] One example of multi-PLD, known as enhanced ASL (eASL), is using seven different post-labelling delay times with modified Hadamard encoding to assess CBF maps.[21, 39, 40] With these multi-delay images, a transit time map and a transit time corrected CBF map can be computed.[41] Research has proven that transit time corrected CBF maps can overcome errors in perfusion maps caused by delayed ATT's.[37]

CBF is an important biomarker when investigating local hypoxia in the brain. Since arterial blood carries oxygen to tissue, ischemic hypoxia is caused by a reduced CBF. However, a normal CBF does not guarantee normoxia as non-ischemic hypoxia occurs despite a sufficient blood flow. Therefore, CBF is an important biomarker of brain oxygenation which should be complemented with other oxygenation parameters.

Vessel Size Imaging

Physiological MRI can also provide other hemodynamic parameters through vessel size imaging (VSI). This type of DSC imaging requires a gradient echo (GRE) combined with spin echo (SE) image acquisitions to simultaneously measure changes in the relaxation rates ΔR2 and ΔR2* caused by a gadolinium-based contrast agent passing through the cerebral vasculature and increasing susceptibility contrast between blood and parenchyma. This is also known as hybrid echo planar imaging (HEPI). Within this technique, the gradient echo signal can be converted to ΔR2* and the spin echo signal can be converted to ΔR2 by:

$$\Delta R2^{*} = \frac{1}{TE_{GRE}} * \log\left(\frac{S(t)_{GRE}}{S(0)}\right) \quad (1)$$

$$\Delta R2 = \frac{1}{TE_{SE}} * \log\left(\frac{S(t)_{SE}}{S(0)}\right) \quad (2)$$

where TE = echo time, S = measured MR signal.[42] The ratio between them can be used to provide information regarding vessel size as sensitivity of SE DSC peaks for capillary-sized vessels, whereas GRE DSC is sensitive to a broader range of vessel sizes with greater sensitivity to larger vessels.[43-45]

Data from previous research has shown that VSI correlates with vessel sizes obtained from histopathology in human gliomas. However, the same data suggests an underestimation of enlarged vessels and an overestimation of capillary sizes using VSI.[23] This finding regarding capillary sizes is consistent with several studies performing a comparison of VSI and vessel sizes obtained from histopathology on tumour models within rats.[46-48] So validation of VSI has occurred, indicating care should be taken when using quantified VSI.

When computing VSI maps out of ΔR2 and ΔR2*, additional information is required to complete this computation. According to Kellner et al.[23] and Chakhoyan et al.[49] VSI can be computed according to equation (3), proposed by Kiselev et al.[42]:

$$Mean\ vessel\ size = 0.867 * \sqrt{rCBV * ADC} * \frac{\Delta R2^*}{\Delta R2^{\frac{2}{3}}} \quad (3)$$

with rCBV = relative cerebral blood volume, ADC = apparent diffusion coefficient. A rCBV map can be derived from the ΔR2* data and is an important biomarker which is widely applied for glioma grading, post-treatment assessment and treatment response.[50-53] CBV measurements can vary for the same type of tissue, within the same patient, scanned with the same MR scanner and protocol. This can be fixed by normalizing CBV measurements to a healthy reference region of interest (ROI). However, this is a time-consuming process and delineation of the ROIs introduce inter-observer variability. Therefore, a standardization of rCBV maps for inter- and intrapatient comparisons was introduced.[54]

To compute VSI maps, another important parameter needs to be computed from the acquired data: the apparent diffusion coefficient (ADC). ADC maps can be acquired by diffusion-weighted imaging (DWI) after applying different b-values, which refer to the influence of gradients on the diffusion-weighted images, in equation (4):

$$S = S_0 * e^{-b*ADC} \quad (4)$$

with S = signal intensity, S0 = signal intensity when no diffusion gradients are used.[55] The value of the ADC represents the diffusion capacity of a specific biological tissue.[56, 57] It follows that ADC maps are a useful tool for in-vivo tumour characterization. Research has established that by using ADC maps, necrotic parts of the tumours can be detected as this tissue has less diffusion obstructions, such as membranes, tight-junctions and cell organelles.[58, 59] Several other studies have found a correlation between ADC and brain tumour grades[60, 61], and an indication that recurrent tumours have lower ADC values than pseudoprogression[62-64], which refers to a progressive lesion with spontaneous improvement within 12 weeks after radiotherapy without any change in treatment. Considering all of this evidence, ADC maps, rCBV maps and VSI maps are important biomarkers regarding hemodynamics of the brain and tumour.

Quantitative Blood Oxygen Level Dependent (qBOLD) Imaging

Another MR imaging technique which provides information regarding haemodynamic and metabolic properties of brain tissue is quantitative blood oxygen level dependent (qBOLD) imaging.[65, 66] This non-invasive MRI method is based on different magnetic properties between oxyhemoglobin and deoxyhemoglobin resulting in the qBOLD model, which describes the transverse MR signal decay in the presence of vasculature. By using the asymmetric spin echo (ASE) sequence at different spin echo times with qBOLD modelling, R2' can directly be measured, while the model also can be used to generate deoxygenated blood volume (DBV) maps.[67] R2' and DBV measurements can be combined to generate a spatial map representing oxygen extraction fraction (OEF), which is an important

biomarker in brain oxygenation.

qBOLD suffers from several limitations or confounds. First, the asymmetric spin echo sequence also measures signal of cerebrospinal fluid (CSF). This contribution to the signal can be removed by using a fluid attenuated inversion recovery (FLAIR) pulse that uses a specific inversion time to null fluids, including CSF.[68] Adding FLAIR to the ASE sequence results in the sequence known as FASE. Second, correction for magnetic field gradients (MFG) is required as R2' can become elevated due to the presence of MFGs resulting in confounded estimates of OEF. This can be done through post-processing the data after acquisition, but also prospectively by combining the ASE technique with gradient echo slice excitation profile imaging (GESEPI). Research has shown that MFG correction and CSF suppression, which resulted in significant decreases in DBV and R2' showing that it removes the CSF contribution to the MR signal, successfully can be applied.[22, 69]

Chemical Exchange Saturation Transfer (CEST) Imaging
Chemical Exchange Saturation Transfer (CEST) is a non-invasive MRI technique which focusses on imaging chemical substances at concentrations that are too low to be detected by MR spectroscopy or imaged by conventional MR imaging. Within this technique, specific tissues can be saturated by a RF pulse, resulting in a reduced or absent MR signal. In CEST, magnetization will be spontaneously transferred from those specific molecules to surrounding water molecules by exchanging 1H protons. By saturating all 1H protons of the surrounding water molecules, the signal difference will be detectable. Specific forms of CEST, such as amine proton transfer (APT), nuclear Overhauser enhancement (NOE) and magnetization transfer (MT) can be measured generating multiple maps.[70-72]

As previously described, gliomas suffer frequently from hypoxia. It is hypothesized that the increased APT signal is usually seen in these regions due to increased tumour protein content in slightly base-like intracellular pH levels.[73] However, this is still debatable as extracellular pH decreases in tumour regions, but due to low extracellular tumour protein content this is not measured by APT CEST.

In summary, different MRI techniques are able to image different parameters of brain and tumour oxygenation. These MRI techniques have already shown to be useful in diagnosis, predicting treatment response and prognosis of patients with gliomas. The next section describes how AI is able to retrieve new features and information of these MR images of different oxygenation parameters and how different AI approaches could combine this information to generate a combined representation of brain and tumour oxygenation.

2.3 Artificial Intelligence approaches

AI applications in gliomas
In terms of applying AI in glioma data, a lot of research has been performed. Several studies focussed on applying radiomics to differentiate between glioblastoma and brain metastases based on MR images.[74, 75] Qian et al. even created a classifier superior to neuroradiologists in terms of accuracy, sensitivity and specificity of differentiating between glioblastomas and solitary brain metastases.[74] Besides differentiating, a plethora of studies has been performed to predict IDH and 1p/19q mutation status in gliomas based on their MR images using AI approaches. These results showed a good discrimination between gliomas with and without IDH and 1p/19q mutations.[76-83]

Standard and advanced MR images have also been used in machine learning models to successfully extract predictive features of gliomas in terms of progression-free survival and overall survival.[84, 85]

Another important post-treatment parameter is pseudoprogression of gliomas. This refers to a progressive lesion with spontaneous improvement within 12 weeks after radiotherapy without any change in treatment.[86] A small and growing body of literature has investigated the potential of machine learning in differentiating between progression and pseudoprogression of gliomas. These studies showed promising diagnostic accuracies (>75%) for the diagnosis of pseudoprogression with their AI models.[87-92] An interesting result of Jang et al. is an inferior accuracy when the models are based on solely imaging or clinical features compared to models based on both features. This emphasizes the importance of combining multiple features and it demonstrates the potential of integrating clinical features as well.[89] Despite this body of literature, applying AI to combine different MR brain oxygenation parameter images into a combined representation has not been explored yet. The next sections describe different AI approaches that could potentially be used to fuse previously described MR brain oxygenation parameter images into a single oxygenation map.

Generative Adversarial Network (GAN)

Combining multiple MR images into a single map is basically translating one image into another image, a process also known as image-to-image translation. Recently, Generative Adversarial Networks (GANs) were proposed as an AI approach to achieve image-to-image translation.[93] The architecture of this network, shown in *Figure 5*, consists of a generator and discriminator that translates images into new images and simultaneously tries to distinguish the real image from the generated image, respectively.

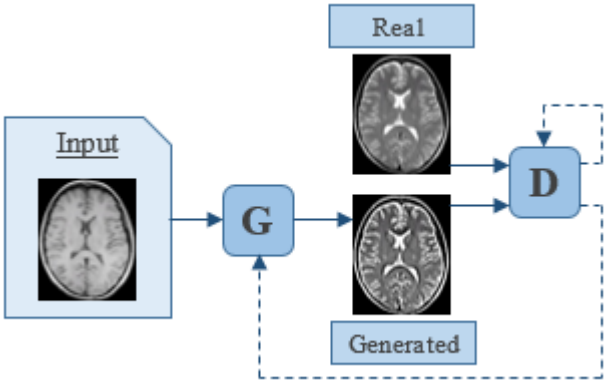

Figure 5: Outline of the GAN with a generator (G) and a discriminator (D). An example of training the model to generate T2 MR images from T1 MR images.

Both parts of the GAN are CNNs. Thus, the discriminator is trained by updating its model parameters when it misclassifies the real data as generated data or the generated data as real data. However, the generator is trained by generating data from the input data and when the discriminator classifies the generated data as generated data, the generator needs to adjust its model parameters to improve its performance. The generator tries to fool the discriminator whereas the discriminator tries to distinguish the generated data from the real data.

In the field of medical image synthesis, multiple applications of GANs have been performed to

translate a modality image into an image of another modality, including MRI to CT synthesis[94-97], CT to MRI synthesis[98], CT to PET synthesis[99, 100] and multi-contrast MRI synthesis[28, 29]. Thus, a GAN could potentially fuse different brain oxygenation MR images into a new image. However, conventional GANs use real data to establish the loss between the real data and the generated data. Unfortunately, when generating a combined representation image, a ground truth image is absent. Recently, CycleGANs have been proposed as a method to deal with unpaired data. This type of GAN uses two generators to generate data from one domain to another and vice versa. Although several studies showed successful applications of CycleGANs using unpaired data to train the model, examples of a ground truth were still required in these studies.[94, 95, 101]

Auto-encoders

Another AI model in the field of deep learning is the autoencoder. This is the most common AI model in deep learning that uses unsupervised learning.[102] Within image analysis, autoencoders are CNNs with a symmetric structure, where the middle layer is a higher-order representation of the data. The first part of the network before the middle layer, also known as the encoder, encodes the input data into a higher-order representation. The part after the middle layer, also known as the decoder, decodes the higher-order representation into an output which is as closely as possible to the input data. The typical structure of an autoencoder with images as input is shown in *Figure 6*.

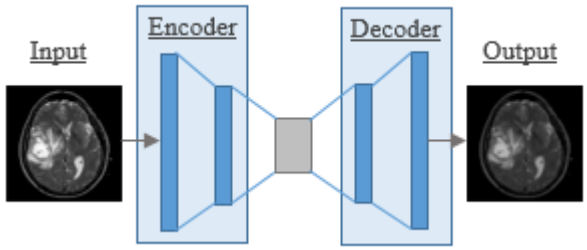

Figure 6: Architecture of an autoencoder network.

Autoencoders have the potential for extracting most relevant features that represents the specific input data. This is done by encoding the input data into a simple representation of the input data. This encoding in the middle layer of the network consists of features of the input data. The decoder checks if these features are representative for the input data as it decodes the encoding into an specific output. When this output data is nearly the same as the input data, the encoding consists of features that are representative for the input data.

Within medical image analysis, autoencoders have also been used to extract features from images.[28] Zhou et al. even used, besides the middle layer, data representations from multiple layers in the autoencoder network to extract features. They applied multiple autoencoders for different MRI techniques to fuse their higher-order data representations to create a new image using a GAN. To combine information of multiple MR images, multiple autoencoders are not required as multiple MR images can be given as input to one autoencoder, trying to regenerate the multiple input data based on their higher-order representations. Several other studies have also used autoencoders for image synthesis.[103-105] Costa et al.[105] and Huang et al.[104] used autoencoders in combination with GANs for image synthesis, while Sevetlidis et al.[103] used an autoencoder to code an MR image into a higher-order representation and use the decoder to

generate an image of another MRI technique. Regarding the fusion of multiple MR images into a single map, the combination of autoencoder(s) with a GAN or using autoencoders to generate a new image based on the higher-order representation of the input MR images are promising methods. However, an example of the new image is required to train these AI models to generate the specific output image.

Clustering

Clustering is an unsupervised leaning method which tries to group data points in a dataset based on their similarities. This process is shown in *Figure 7*. Within the groups, data points should have similar features, while data points in different groups have highly dissimilar features. There are many methods to perform clustering of data with K-means clustering being the most well-known algorithm. This technique tries to find a predefined number k of clusters. This is done by allocating every data point to the nearest centre of a cluster. When all new data points have been assigned to a cluster, the cluster centres are updated. This process will be repeated until the clusters remain unchanged or the maximum number of iterations has been reached.[106]

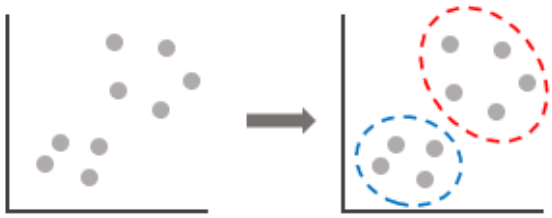

Figure 7: Clustering of data points based on similarities.

Every method of clustering has its own limitations depending on the data distribution as clustering performance strongly depends on the data distribution. Therefore, it is very useful to inspect the data distribution in advance of choosing and performing a clustering approach. However, clustering can also be done with more than three parameters per data point resulting in higher-dimension scatter plots in which the data distribution cannot be visualized in a 3D space.[107] Besides, the performance of several clustering methods, including k-means clustering, heavily depends on the initial starting conditions.[108]

Multiple studies have already used clustering in genetic data of glioma patients.[109, 110] Those studies proved that clustering is a valuable contribution in diagnosis and prognosis of gliomas. Interestingly, the clustered glioma data showed that genetic data is more reflective of subtypes than histological class.[110] Other studies applied clustering to genetic data and prognostic data showing genetic data strongly predicts survival.[111, 112] This demonstrated importance of molecular information of gliomas was also taken into account in the latest version of the WHO Classification of CNS tumours.[5]

Despite clustering in glioma data having mainly been performed on genetic data, it could potentially be applied at imaging data of gliomas as well. When clustering earlier discussed MRI oxygenation parameters, different types of brain oxygenation could be identified including healthy oxygenation and different types of hypoxia. These different types of oxygenation could be visualized in a single map. However, clustering data with multiple parameters results in a data distribution that cannot be visualized. Therefore, clustering could be an effective method to combine multiple MRI oxygenation

parameters into a single map, but it remains unknown if the clustering could be performed better.

In the next sections of this literature study, three well-known clustering methods were reviewed: centroid-based clustering, density-based clustering, and hierarchical clustering. All three clustering methods try to group the data points into clusters in a way that the data points within a cluster are similar, but are dissimilar in contrast to data points in other clusters.

In the case of centroid-based clustering, the number of clusters (*k*) is required to be set in advance of the clustering. This algorithm starts by assigning *k* random data points as the centers of clusters. Then the distance from each center of the cluster to a new data point is measured and the new data point is added to the nearest cluster, resulting in an updated center of the cluster. This process is repeated until all data points are assigned to a cluster.

Centroid-based clustering is relatively simple and fast method. However, the results are strongly dependent on the initial data points which are assigned as the start of each cluster. This could be optimized by performing the clustering process multiple times with varying initial data points as start of the clusters. The main disadvantage of centroid-based clustering in regards of the purpose of this study is that the number of clusters needs to be manually set in advance of the clustering. This is information that is not known in advance, and moreover, varies between patients. An overview of the advantages and disadvantages are shown in *Table 1* .[113-115]

Table 1: Advantages and disadvantages of centroid-based clustering.

Advantages	Disadvantages
• Easy to implement; • Relatively fast method; • Can handle large amount of data;	• Number of clusters needs to be set manually in advance of clustering; • Centroids can be dragged by outliers; • Results are dependent on initial values → this can be optimized to guarantee the best results; • Struggles with data clusters with varying densities; • Struggles with non-spherical or non-elliptical cluster shapes.

In contrast to centroid-based clustering, density-based clustering aims to separate clusters with high density from clusters with low density. The most well-known density-based clustering algorithm is Density-Based Clustering of Applications with Noise (DBSCAN). Within this algorithm, two parameters need to be set in advance of the clustering: the neighbourhood distance ε, and the minimum number of points (*minPoints*) which should be present in the neighbourhood of a data point to start a cluster.

This method starts with a randomly selected data point. By using ε and *minPoints*, the algorithm checks if sufficient data points are present in the neighbourhood of the starting data point. When this is not the case, that data point will be labelled as noise. Otherwise, this data point will be labelled as part of cluster and all data points within its neighbourhood will be assigned to that cluster as well. For each of these neighbour data points, ε and *minPoints* are used again to investigate if their surrounding data points can be assigned to that cluster as well. This process will be repeated until all

data points in the neighbourhood have been analysed and assigned as part of the cluster or labelled as noise. When this process is completed, a new unlabelled data point will be investigated the same way to determine if it should be labelled as a new start of a cluster or as noise. The algorithm will repeat this until all data points have been labelled as part of a cluster or as noise.

Due to this clustering technique, the algorithm is able to find arbitrary-shaped clusters and handle noisy data. However, clusters are not always defined by their density and this method struggles with high-dimensional data. An overview of the advantages and disadvantages of this technique is given in *Table 2*.[114, 116]

Table 2: Advantages and disadvantages of density-based clustering.

Advantages	Disadvantages
• Number of clusters do not need to be set in advance of clustering; • Is able to find arbitrary-shaped clusters; • Robust to outliers.	• Not able to separate different clusters with similar densities; • Not able to group data points into a cluster when the group has varying densities; • Struggles with high-dimensional data;

Regarding hierarchical clustering, this algorithm can be performed by two different methods:

- Agglomerative: The algorithm starts with defining every data point as a separate cluster. By measuring the distance between all clusters, the algorithm determines the smallest distance and merges these two clusters together into a new cluster. This process will be repeated until all data points are merged into one cluster;
- Divisive: The algorithm starts with one cluster containing all data points. By measuring the distance between all clusters, the algorithm determines the greatest distance and splits the cluster into two clusters;

Both methods result in a dendrogram: a tree-based representation of merging and splitting of clusters. Within this graph, the optimal number of clusters can be determined since the largest vertical distance without merging or splitting of clusters represents the most dissimilar clusters. At this level in the dendrogram a horizontal line can be drawn and the number of intersections with vertical lines represents the number of clusters.

To determine which clusters need to be merged or split, different distance metrics and linkages can be used in hierarchical clustering, which respectively measures the distance between data points and measures the distance between clusters. The most well-known linkage options are: single linkage, average linkage, complete linkage, and ward linkage. Within single linkage the algorithm uses the smallest distance between two points, in which each point belongs to two different clusters. With average linkage the algorithm uses the average distance between all combinations of data points of the two different clusters. With complete linkage the algorithm uses the greatest distance between two points, in which each point belong to two different clusters. In contrast to other linkages, ward linkage analyzes the variance of the clusters. With ward linkage the algorithm tries to achieve the least increase in total variance by using the Ward variance minimization algorithm:

$$d(u,v) = \sqrt{\frac{|v|+|s|}{T}d(v,s)^2 + \frac{|v|+|t|}{T}d(v,t)^2 - \frac{|v|}{T}d(s,t)^2} \quad (5)$$

where v is an unused cluster and u is the newly joined cluster consisting of clusters s and t.

A simplified overview of the different linkages is shown in *Figure 8*. To measure the distance between two data points, different distance metrics result in different clustering outcomes. Two classic distance metrics are Euclidean and Manhattan, where the distance is measured by calculating the square root of the sum of the square differences and by summing the vertical and horizontal distance between the two points, respectively. An overview of the advantages and disadvantages regarding hierarchical clustering is shown in *Table 3* .[114, 115, 117]

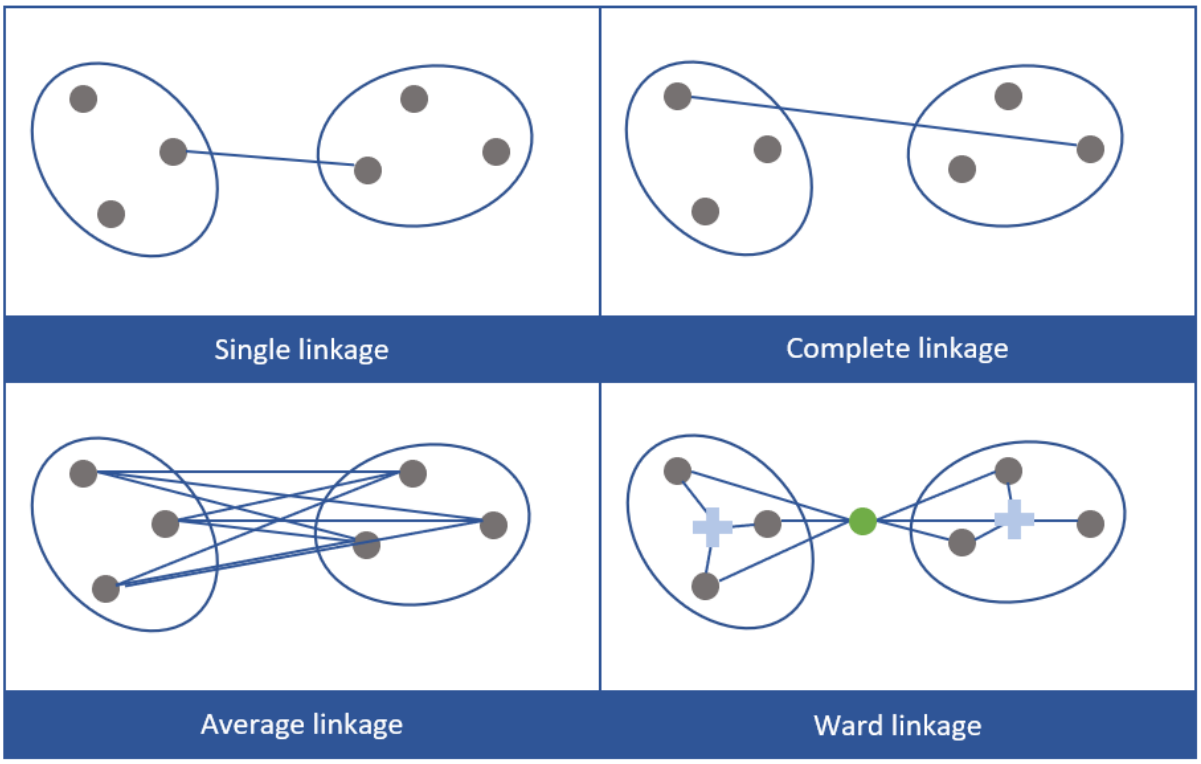

Figure 8: Overview of how different linkages measure the distance between two clusters.

Table 3: Advantages and disadvantages of hierarchical clustering.

Advantages	Disadvantages
• Easy to implement; • A dendrogram is created to determine the optimal number of clusters, which is very informative; • No a priori knowledge about the number of clusters is required.	• Can't undo what is done; • Time-complexity → this can be fixed by using extra computational power of BIGR; • Sensitive to noise. This depends on which distance metric is used → this can be optimized by comparing results of different metrics and linkages; • Can be difficult to identify correct number of clusters based on the dendrogram.

Hyperparameter optimization

The previous sections have shown different AI methods that could be used to combine different MRI brain oxygenation parameters into a single map. However, these models have many settings which need to be set in advance of the (training) process, including learning rate of the training process. These settings, called hyperparameters, are not adjusted during the training process in contrast to the model parameters.

Many approaches have been proposed to optimize these hyperparameters to achieve the highest performance of the AI model. These approaches can be divided into two groups: exhaustive search of hyperparameter space and Sequential Model-Based Optimization (SMBO). The two most well-known exhaustive search approaches are grid search and random search. Grid search uses a predefined set of values for each hyperparameter individually and tries every possible combination of these predefined hyperparameter values. In contrast to grid search, random search tries combinations of randomly generated hyperparameter values. As shown in *Figure 9*, the main advantage of random search compared to grid search is that random search results in more knowledge regarding the impact of a single hyperparameter on the model performance. For example, when both optimization strategies are performed with nine combinations each, grid search tries three different values for every hyperparameter, whereas random search tries nine different values for every hyperparameter. However, both methods are still computationally expensive as they do not take previous knowledge on hyperparameter value combinations into account when trying a new combination.[118]

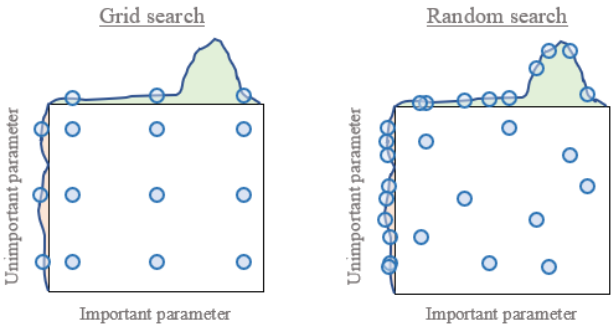

Figure 9: Layout of different hyperparameter values during grid search and random search. In this example, random search results in more knowledge regarding the importance of different hyperparameters.

In contrast to an exhaustive search of hyperparameter space, SMBO chooses its new set of hyperparameter values based on a surrogate model. This is a probability representation of the true model performance for different hyperparameter values. After every new combination of hyperparameter values, the probability model is updated and approaches the true performance function more and more closely resulting in the location of the global optimum of all hyperparameter value combinations. This process is shown in *Figure 10*. This method can be performed by different processes with Gaussian Process and Tree-structured Parzen Estimator being the most well-known.[119-121] The main disadvantages that still remain within these processes is that these algorithms still have their own hyperparameters that needs to be set manually and previous knowledge is still required to predefine the range of hyperparameter values.

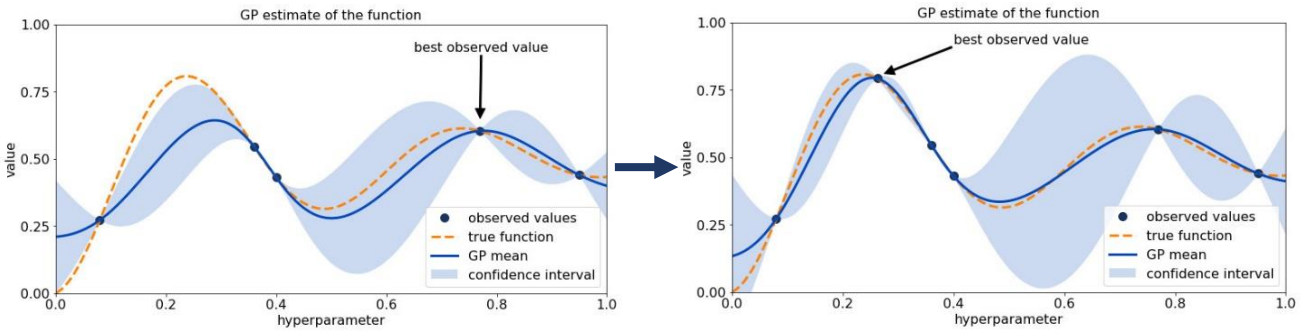

Figure 10: Process of hyperparameter optimization of a SMBO method. A new hyperparameter value and its model performance results in a better approach of the true performance function.

2.4 Conclusion

The aim of the current study was to give an overview of different MRI methods to assess brain oxygenation and different AI approaches to fuse these MR images into a complete brain oxygenation map. All of the described MRI techniques contain important information regarding brain oxygenation and therefore should be included when combining multiple MR images to generate a single brain oxygenation map. Due to the absence of a ground truth image, a GAN would not be preferable for this research purpose. While auto-encoders have the potential to be a useful tool for feature extraction if needed, clustering based on those MRI techniques is an AI method which could identify different states of oxygenation that could be visualized in a single image. Hierarchical clustering is the most promising clustering algorithm since a priori knowledge is not required and the number of clusters present in the tumour is also not known in advance. In addition, a dendrogram could be insightful to determine the number of clusters and the clustering performance can be optimized by testing different metrics.

This review has also shown that when such an AI project will be performed, it is important to use a SMBO method to optimize the hyperparameters of the model and take the limitations of each MRI technique into account. In addition, it is necessary to check the impact of each MRI method on the resulting image to guarantee no useless data and computational power will be used when generating these images in the clinical practice.

Chapter 3
Methods

Chapter 3 Methods

3.1 Patient selection

The data in this research was retrieved from patients with brain tumours treated in the Erasmus Medical Centre in Rotterdam. Patients were included when they met the following criteria:

- age ≥ 18 years;
- eligible for resection of primary brain tumour or brain metastasis;
- informed consent was given according to ICH-GCP.

Patients were excluded when they met the following exclusion criteria:

- contra-indication for MRI;
- received chemotherapy before or during MRI;
- not possible to give informed consent.

All included patients underwent MR imaging according to the MR imaging protocol. Subsequently, these patients underwent resection of the tumour in which biopsies were taken at multiple locations within the tumour.

3.2 Image acquisition

The brain MR imaging protocol, named ITEM (Imaging of Tumour Environment Mapping), consists of multiple sequences and has been designed to assess structural and physiological information regarding the brain tumour and surrounding brain tissue. MRI scanning of the included patients was performed on a 3T scanner (Discovery750, General Electric, Chicago, USA) with a 32-channel head coil according the ITEM scan protocol. The first part of this protocol included: T1-weigthed imaging (TE/TR = 2.1/6.1 ms, FOV = 256 mm, 352 slices), T2/FLAIR-weighted imaging (TE/TR = 111.4/6002 ms, voxel size = 1.1x1.1x1.6 mm^3, matrix size = 224x224x264), DWI with three b-values of 0, 10, and 1000 s/mm^2 (TE/TR = 63/5000 ms , voxel size = 1x1x3 mm^3), eASL (TE = 10.8 ms, slice thickness = 3.5 mm), APT-CEST (TE/TR = 3.2/7 ms, FOV = 220x180x42 mm^3, voxel size = 1.7x1.7x3 mm^3, matrix size = 128x104x14 and FASE (TE/TR = 74/8000 ms, slice thickness = 2.0). After injecting 7.5 ml Gadovist with 12 ml NaCl into the patient, the second part of the protocol was performed, which included: T2-weighted imaging (TE/TR = 8.4/0.14 ms, voxel size = 0.46x0.46x5.00 mm^3), T1-weigthed imaging (TR = 6.1 ms, voxel size= 1x1x1 mm), and HEPI (TE/TR (GRE) =18.6/1500 ms, TE/TR (SE) = 69/1500 ms, voxel size = 1.88x1.88x4.00 mm^3, number of repetition = 122 times and brain coverage of 15 slices (24)). 5 minutes prior to the HEPI sequence a second bolus of Gadovist was injected into the patient. The complete ITEM MR imaging scanning protocol has a duration of approximately 60 minutes and its outline is shown in *Figure 11*. Further details of the image acquisition are described in *Appendix A*.

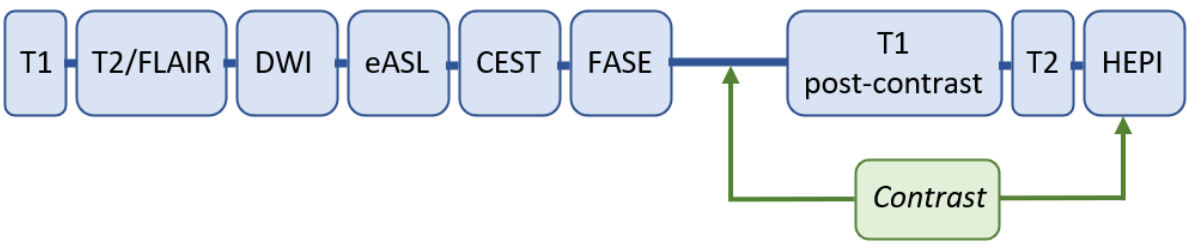

Figure 11: Outline of the ITEM MR imaging protocol.

3.3 Data processing

The T1-weighted images and T2/FLAIR images are derived from the T1-weighted and T2/FLAIR image acquisition, respectively. These images contain mainly structural information regarding brain tissues. Apparent Diffusion Coefficients (ADC) maps are derived from the data acquired by the DWI sequence following the equation:

$$S = S_0 * e^{(-b*ADC)} \quad (4)$$

with S = signal intensity, S0 = signal intensity when no diffusion gradients are used.[55] Furthermore, the transit-time corrected CBF maps are computed based on the eASL image acquisition. From the CEST imaging sequence APT maps are derived and from the FASE sequence, R2' maps and deoxygenated blood volume maps could be derived. By using both R2' and DBV measurements, a spatial map of the oxygen extraction fraction can be calculated by equation (6):

$$OEF = \frac{R_2'}{DBV * \gamma * \left(\frac{4}{3}\right) * \pi * \Delta\chi_0 * Hct * k} \quad (6)$$

with γ = nuclear gyromagnetic ratio, Hct = blood hematocrit level, $\Delta\chi_0$ = susceptibility between completely deoxygenated and completely oxygenated red blood cells.[122]

The T2-weighted images and post-contrast T1-weigthed images are generated based on the T2-weigthed and T1-weighted image acquisition performed after contrast injection. The added value of T2-weighted imaging compared to T1-weighted imaging, is that T2-weighted imaging can be used to identify peritumoral edema and non-enhancing tumours as those are regions are hyperintense on T2-weigthed images. In addition, post-contrast T1-weigthed images are able to show enhancing regions in the tumour area, indicating a disrupted blood-brain barrier.[123]

The final sequence in the ITEM MR imaging protocol is HEPI. ΔR2 and ΔR2* values were derived from the measured MR signals by the following equations:

$$\Delta R2^* = \left(\frac{1}{TE_{GRE}}\right) * \log\left(\frac{S(t)_{GRE}}{S_0}\right) \quad (1)$$

$$\Delta R2 = \left(\frac{1}{TE_{SE}}\right) * \log\left(\frac{S(t)_{SE}}{S_0}\right) \quad (2)$$

with TE = echo time, S = measured MR signal.[42] Based on the ΔR2* maps, relative cerebral blood volume maps can be generated by the following equation:

$$rCBV = \int_{t_0}^{t_1} \Delta R_2^*(t)\, dt \quad (7)$$

The ΔR2, ΔR2*, rCBV values in combination with the previously acquired ADC values were used to compute vessel size maps according to equation (3) :

$$Mean\ vessel\ size = 0.867 * \sqrt{rCBV * ADC} * \left(\frac{\Delta R2^*}{\Delta R2^{\frac{3}{2}}}\right) \quad (3)$$

with rCBV = relative cerebral blood volume, ADC = apparent diffusion coefficient.

3.4 Image registration

To align all images into one coordination system, image registration can be performed. In this research, image registration was necessary due to the different acquisition sequences generating images with different resolutions in different coordinate systems. In order to prevent loss of data, all maps acquired by the ITEM MR imaging protocol were registered to the T1 post-contrast image as this map has the highest resolution. By performing image registration, all included images were transferred to the same space and were sampled so they have the same number of voxels as the T1 post-contrast image. It is necessary that all maps align such that the voxels in the different images all occupy the same physical spot as each voxel is analyzed during the clustering as a single data point containing multiple values, each value representing the same voxel in a different map.

However, by registration of all images to the image with the highest resolution, the images with lower resolutions are upsampled and therefore generate fake data by interpolating between true data points. To investigate this effect on the clustering results, the T1 post-contrast map was registered to the vessel size map generated by the HEPI sequence as this map has the lowest resolution. Then all other maps were registered to this downsampled T1 post-contrast map, resulting in all maps being downsampled so the number of voxels is the same for each map and all maps are aligned with each other.

3.5 Image segmentation

In a first experiment, clustering was performed to distinguish between white matter, gray matter, and cerebrospinal fluid to verify clustering as an appropriate approach for further image analysis. To check if the clustering approach was able to identify healthy white matter, gray matter, and cerebrospinal fluid as separate brain tissues, the voxels needed to be labelled. Therefore, segmentation of white matter, gray matter, and cerebrospinal fluid of the healthy hemisphere was performed to create masks and assign each voxel as white matter, gray matter, or cerebrospinal fluid. Segmentation was performed on the T1-weighted image with the FAST tool (v4.0) of FSL resulting in probability maps for each type of healthy brain tissue. Since these masks were used a label to validate the clustering results, only voxels with a probability of 1.0 were included in the tissue masks used for this analysis.

When clustering was verified as a suitable approach, the main experiment was performed by clustering of brain tumour voxels to identify and locate different oxygenation states within the tumour. Segmentation of the brain tumour was performed manually based on the T1, T2/Flair, T2 and T1 post-contrast images in ITK-SNAP.[124] Enhanced areas of the tumour were included in the

segmentation. These segmentations were checked by an experienced neuroradiologist.

3.6 Algorithm parameters

In this research, clustering was used as AI method to create a combined representation of multiple oxygenation parameters acquired by MRI. Based on literature findings, agglomerative hierarchical was chosen as clustering method since no a priori knowledge was required and the number of clusters can be derived from the dendrogram in contrast to centroid-based and density-based clustering. In addition, the clustering performance of hierarchical clustering can easily be optimized by testing different parameter settings.

Regardless which clustering method was chosen, all algorithms have many parameters that need to be set in advance of the clustering. These setting strongly affect the outcome of the clustering. Therefore, the first step in this research was to perform the hierarchical clustering multiple times combining different linkages and distance metrics to compare the clustering results and determine which linkage and distance metric result in the highest clustering performance. In this step clustering performed 7 times with the settings shown in *Table 4*. Note that Ward linkage exclusively can be performed with Euclidean distance.

Table 4: Combinations of linkages and distance metrics that were used when performing clustering multiple times.

	Linkage	Distance metric
1	Single	Euclidean
2	Complete	Euclidean
3	Average	Euclidean
4	Ward	Euclidean
5	Single	Manhattan
6	Complete	Manhattan
7	Average	Manhattan

To know which settings provide the best clustering results, it is necessary to know if the clustering algorithm clustered the data in the correct groups. For this analysis the masks of the white matter, gray matter, and cerebrospinal fluid of the healthy hemisphere were used. The white matter, gray matter, and cerebrospinal fluid voxels of the T1 and FLAIR images of patient 001 were included for this analysis. For this analysis, only 80.000 voxels of each tissue were included due to the large required computational power when including all voxels. Since the aim was to separate the data into a cluster with white matter voxels, a cluster with gray matter voxels, and a cluster cerebrospinal fluid voxels, the clustering algorithm was set to group the data into three clusters. The clustering algorithm was programmed by using Python version 3.6.8 (Python Software Foundation. Python Language Reference. Available at http://www.python.org). An example of a Python script used in this research to cluster image data with ward linkage and Euclidean distance is shown in *Appendix B*. After clustering, the data points were shown in a scatter plot with their corresponding T1 and T2/FLAIR values on the x- and y-axis, and their assigned colour will show which cluster they have been assigned to. In addition, the clustered groups were checked for how well they matched the groups of white matter voxels, gray matter voxels, and cerebrospinal fluid voxels.

3.7 Reducing computational power

An important disadvantage of clustering algorithms, especially hierarchical clustering, is the large computational complexity when datasets are extremely large. Therefore, the second step in this research was to reduce the required computational power since the size of the original T1 post-contrast image is 256x256x320, resulting in nearly 21 million voxels that will be included for every patient when performing clustering of white matter, gray matter, and cerebrospinal fluid voxels. To reduce this number of voxels and the computational power needed, solely voxels of the healthy hemisphere were included by using the previously discussed masks of white matter, gray matter, and cerebrospinal fluid voxels. In addition, the data type of the intensity values of the T1 and T2/FLAIR were compressed by transforming the float64 values to float16 values. The clustering results of these different data types in Python were compared in terms of running time, maximum memory required and how it affects the result of clustering white matter, gray matter, and cerebrospinal fluid.

3.8 Tumour clustering

The next step in this research was to apply the hierarchical clustering algorithm and its optimal parameter settings (linkage and distance metric) on patient data. For this analysis, the segmentation of the tumours are used to select the voxels that are clustered. At first, a dendrogram is generated to determine the number of clusters present in the image data. A Python script used in this research to generate a dendrogram is shown in *Appendix C*. In this study, the clustering is performed several times in Python with varying MRI maps included to determine the impact and relevance of these maps on the clustering results. The following clustering methods of the tumour voxels are performed:

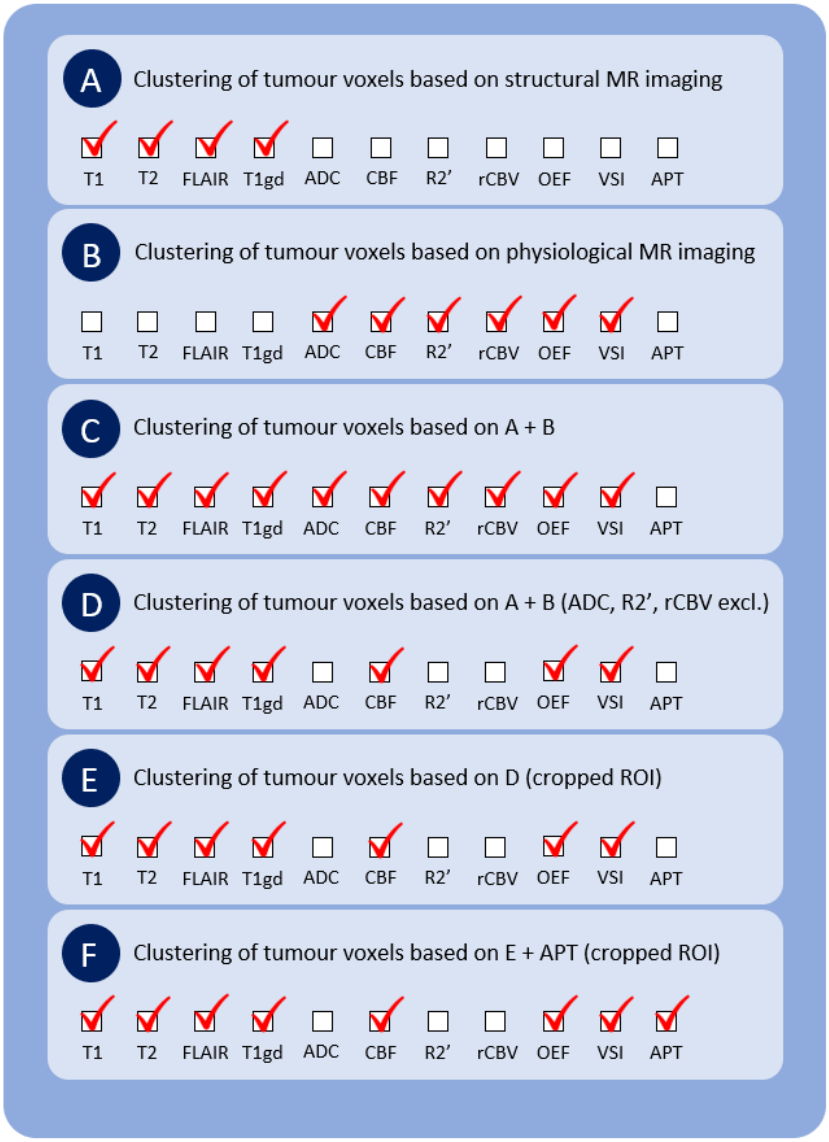

Figure 12: Overview of which maps were included in which clustering analysis.

3.8 Analysis and data visualization

Clustering results per tumour and per analysis were overlaid on T1-weighted images with different colours per cluster for visual inspection of clustering with different inputs.

To analyze what the different clusters represent regarding brain oxygenation and hypoxia, box plots were used to visualize the values of the oxygenation parameters per cluster. The values of each oxygenation parameter were normalized by the following equation:

$$X_n = \frac{X_0 - \mu}{\sigma} \quad (8)$$

with X_n=normalized value in MR image X, X_0=original value in MR image X, μ=mean value of MR image X, and σ=standard deviation of values in MR image X.

Chapter 4
Results

Chapter 4 Results

4.1 Patient characteristics

In this study 3 patients with brain tumours that met the inclusion criteria were included. The patient characteristics including the type of brain tumour based on histological analysis are shown in *Table 5*.

Table 5: Patient characteristics

Patient number	Gender	Age [years]	Histology of brain tumour
001	male	71	Anaplastic oligodendroglioma, WHO grade II
002	female	40	Oligodendroglioma
003	female	52	Metastasis lung carcinoma

4.2 Algorithm parameters

The results for clustering of healthy white matter, gray matter, and cerebrospinal fluid using different linkages and distance metrics are shown in *Figure 13* and *Table 6*.

From the scatter plots, it can be seen that using the single linkage results in clustering nearly all data points into one cluster. Average linkage also results in a poor clustering as there are two large clusters made and one very small cluster. Closer inspection of *Table 6* shows that single linkage clustered nearly all data points into one cluster, which was also seen in *Figure 13. Table 6* also shows that using the average linkage, with both Euclidean and Manhattan as distance metric, results in a reasonable separation of white matter and gray matter voxels from cerebrospinal fluid voxels. However, this linkage metric is not able to separate white matter from gray matter into two different clusters. The combination of ward linkage and Euclidean distance shows the best clustering results based on *Figure 13* and *Table 6* in terms of distinguishing white matter voxels, gray matter voxels, and cerebrospinal fluid voxels from each other.

The results of the clustering with the downsampled T1 and FLAIR maps are shown in *Figure 14* and *Table 7*. As seen in this table and scatter plot, the clustering algorithm was still able to group white matter voxels, gray matter voxels, and cerebrospinal fluid voxels into three separate clusters based on the downsampled maps. *Table 7* shows that the algorithm clustered nearly all cerebrospinal voxels into a single cluster, excluding all white matter and gray matter voxels. However, still a reasonable part of the gray matter voxels end up in the cluster which contains nearly all white matter voxels. In *Figure 14* can be seen that the border between the gray matter voxels and white matter voxels is indeed not very distinctive.

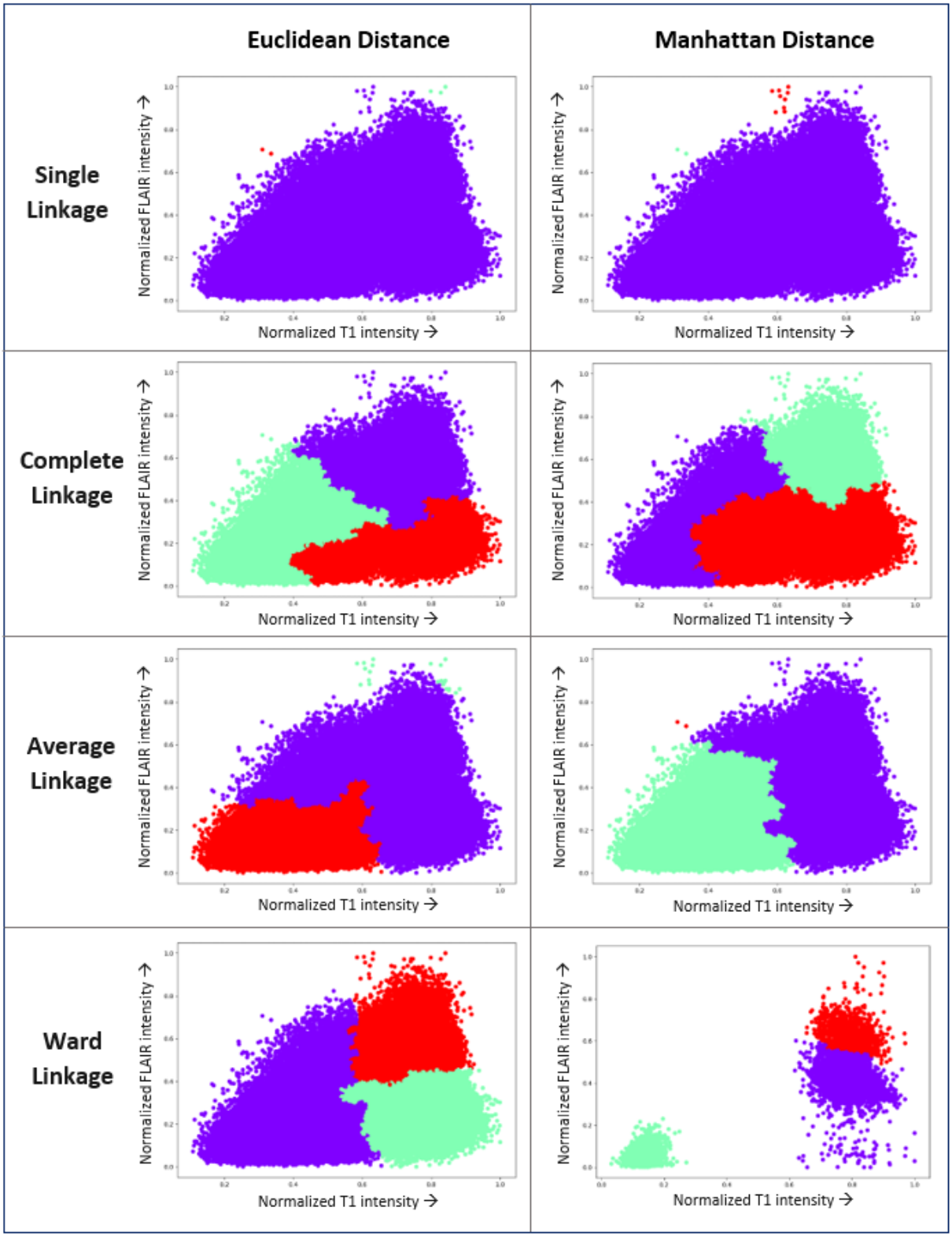

Figure 13: Scatter plots of the clustering done with different combinations of linkages and distance metrics. Each data point was assigned to a cluster by using colours that represent a specific cluster.

Table 6 : Overview of which brain tissue voxels were clustered in which cluster by using different combinations of linkages and distance metrics.

Distance metric	Linkage	Cluster	No. of gray matter voxels	No. of white matter voxels	No. of cerebrospinal fluid voxels	No. total voxels in cluster
Euclidean	Single	1	3	0	0	3
		2	0	0	2	2
		3	79.997	80.000	79998	239995
Euclidean	Complete	1	478	2163	66445	69086
		2	2477	63499	10956	93982
		3	77045	14338	2599	93982
Euclidean	Average	1	13	0	9	22
		2	186	512	69532	70230
		3	79801	79488	10459	169748
Euclidean	Ward	1	6968	79261	764	86993
		2	72911	543	693	74147
		3	121	196	78543	78860
Manhattan	Single	1	0	0	2	2
		2	0	0	9	9
		3	80000	80000	79989	239989
Manhattan	Complete	1	71445	528	328	72301
		2	7970	79466	29293	116729
		3	585	6	50379	50970
Manhattan	Average	1	192	317	77889	78398
		2	0	0	2	2
		3	79808	79683	2109	161600

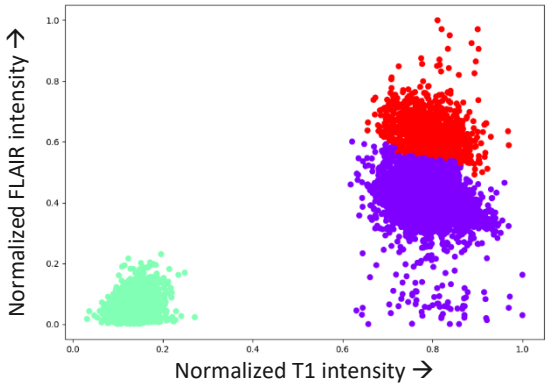

Figure 14: Scatter plot of the clustering performed on the downsampled/registered T1 weighted and T2/FLAIR weighted images with ward linkage and Euclidean distance.

Table 7: Overview of which brain tissue voxels were clustered in which cluster when applying ward linkage and Euclidean distance on the downsampled/registered registered T1 weighted and T2/FLAIR weighted images

Cluster	No. of gray matter voxels	No. of white matter voxels	No. of cerebrospinal fluid voxels	No. total voxels in cluster
1	0	0	3180	3180
2	1145	9	0	1154
3	521	5457	3	5981

4.4 Reducing computational power

MRI maps derived from the image acquisition were included as nifti files in which the data points were represented as float64 values. To reduce computational power, the data points were transformed to float32 values and float16 values. The results of this analysis were shown in *Figure 15*, *Table 8* , and *Table 9*. As can be seen from *Table 8* , changing the data type does not reduce the maximum required memory or running time. The most striking result to emerge from *Figure 15* and *Table 9* is that float32 and float64 values result in exactly the same clustering result, but with float16 values the clustering results differs. Specifically the original T1 and FLAIR images with float16 values result in a worse clustering result compared to that with float32 and float64 values since the algorithm had a reduced performance in distinguishing white matter voxels and gray matter voxels, as can be seen in *Table 9*.

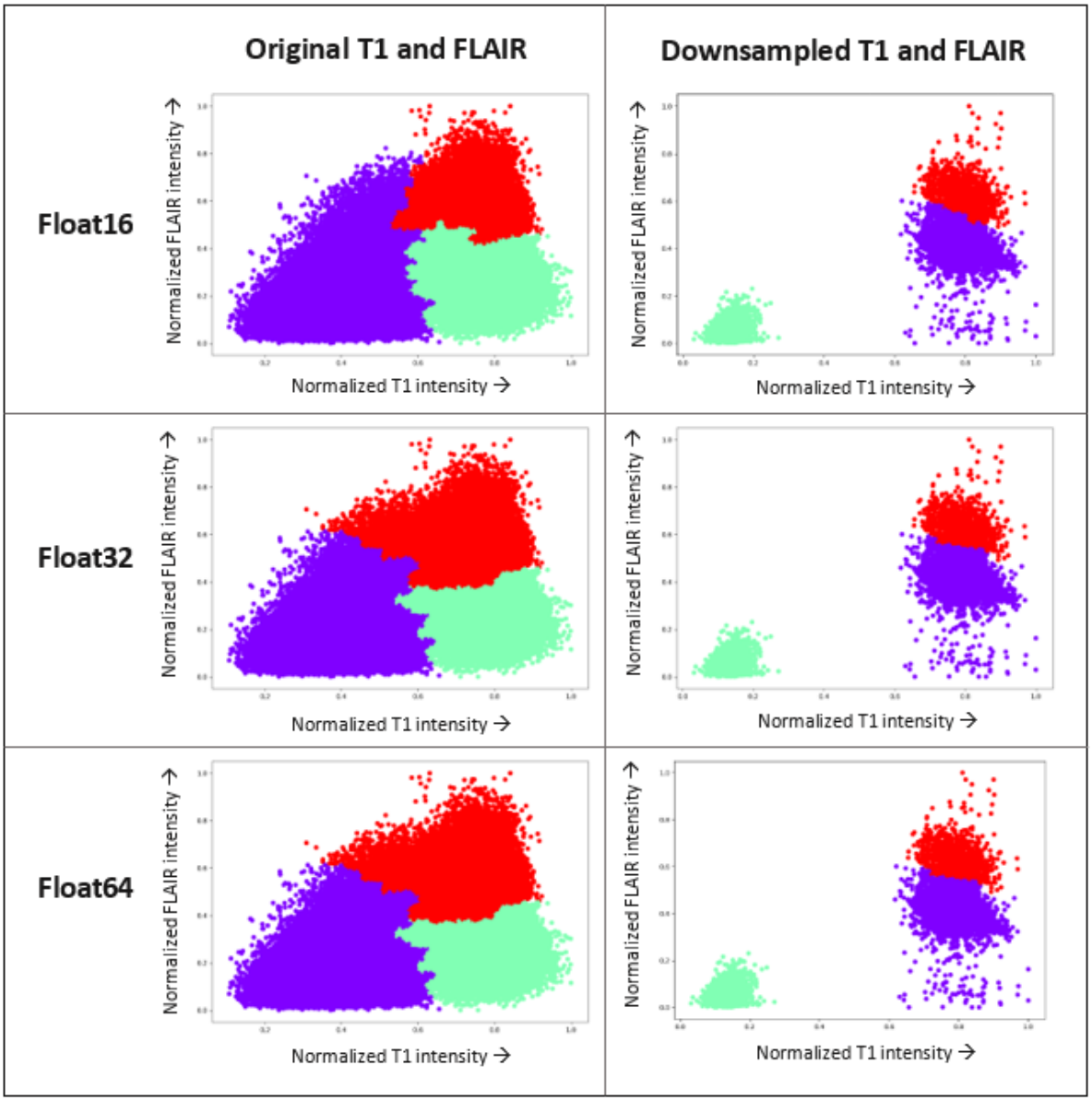

Figure 15: Scatter plots of the clustering done with different data types for the original high resolution T1 weighted and T2/FLAIR weighted images, and the downsampled T1 weighted and T2/FLAIR weighted images.

Table 8: Running time and maximum memory for clustering with different data types on the original high resolution and downsampled T1 weighted and T2/FLAIR weighted images.

Data type	Maps resolution	Maximum memory [GB]	Duration [min]
Float16	Original	432.3	96
	Downsampled	1.6	<1
Float32	Original	432.3	81
	Downsampled	1.6	<1
Float64	Original	432.3	85
	Downsampled	1.6	<1

Table 9: Overview of which voxels were clustered in which cluster when performing clustering with different data types on the original high resolution and downsampled T1 weighted and T2/FLAIR weighted images.

Data type	Maps resolution	Cluster	No. of gray matter voxels	No. of white matter voxels	No. of cerebrospinal fluid voxels	No. total voxels in cluster
Float16	Original	1	12135	79773	671	92579
		2	67669	90	666	68425
		3	196	137	78663	78996
	Downsampled	1	0	0	3180	3180
		2	1186	18	0	1204
		3	480	5448	3	5931
Float32	Original	1	4628	78233	535	83396
		2	75233	1536	2117	78886
		3	139	231	77348	77718
	Downsampled	1	0	0	3180	3180
		2	1145	9	0	1154
		3	521	5457	3	5981
Float64	Original	1	4628	78233	535	83396
		2	75233	1536	2117	78886
		3	139	231	77348	77718
	Downsampled	1	0	0	3180	3180
		2	1145	9	0	1154
		3	521	5457	3	5981

4.5 Tumour clustering

The different clusters and their locations within a tumour are visualized by using different colours for each cluster on the T1 image, shown in *Figure 16, 17, and 18* for patient 001, 002, and 003, respectively. The boxplots of each oxygenation parameter are shown for the corresponding clusters in *Figure 19, 20, and 21* for patient 001, 002, and 003, respectively.

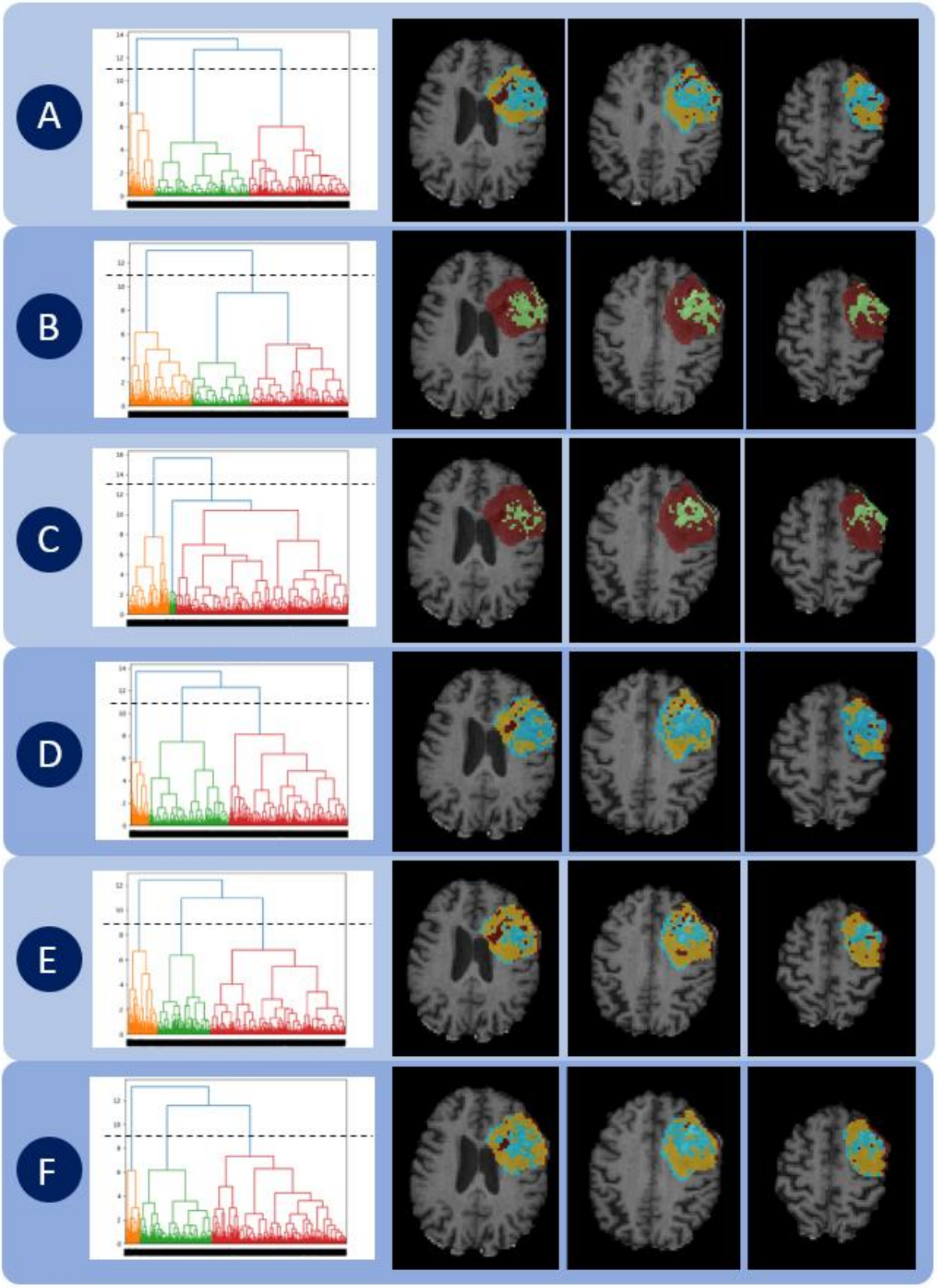

Figure 16: Dendrogram and the location of the clusters in slice 7, 10, and 15 within patient 001 for each clustering method (letters correspond to letters explained in Chapter 3 Methods)

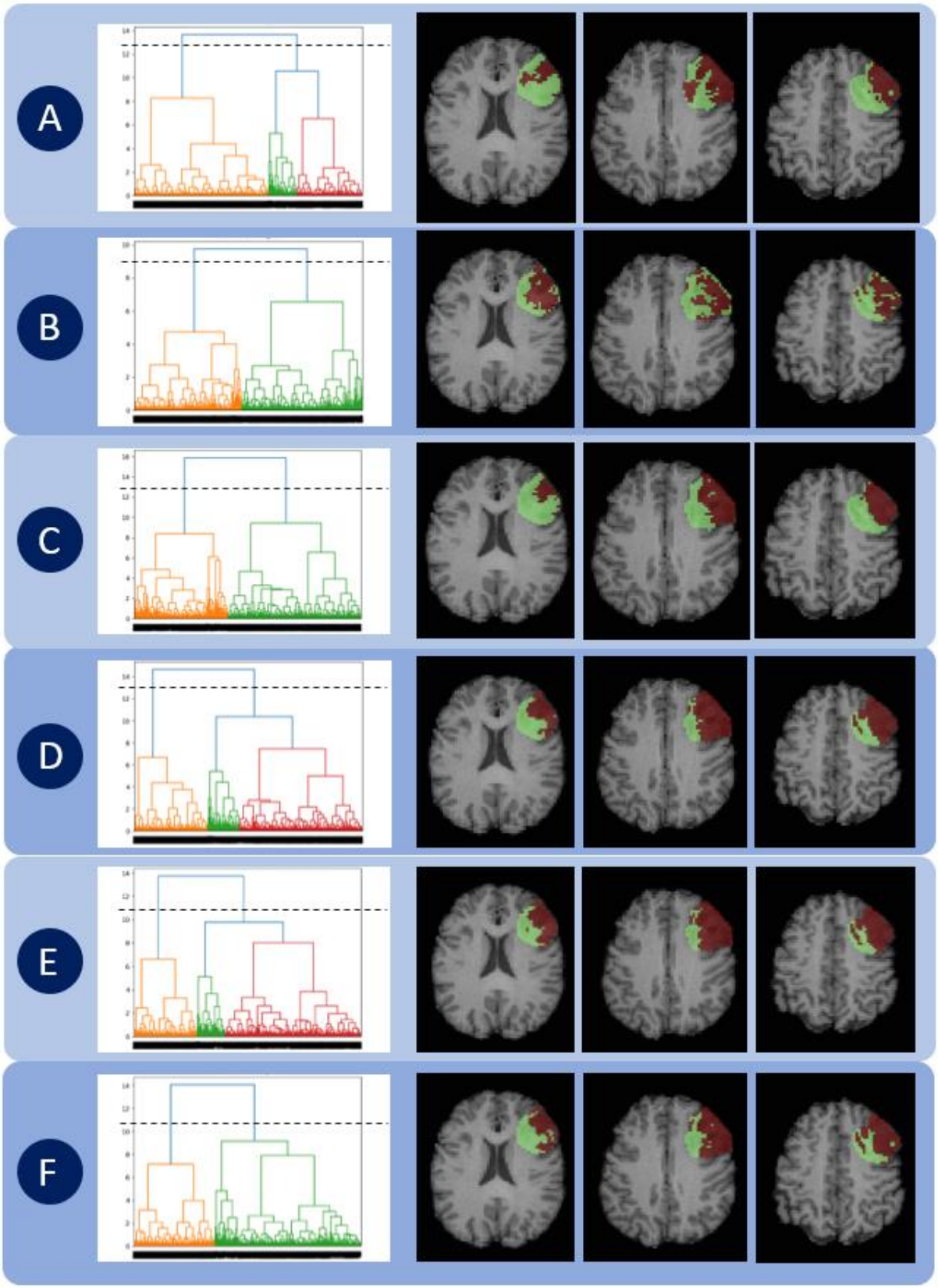

Figure 17: Dendrogram and the location of the clusters in slice 9, 13, and 16 within patient 002 for each clustering method (letters correspond to letters explained in Chapter 3 Methods)

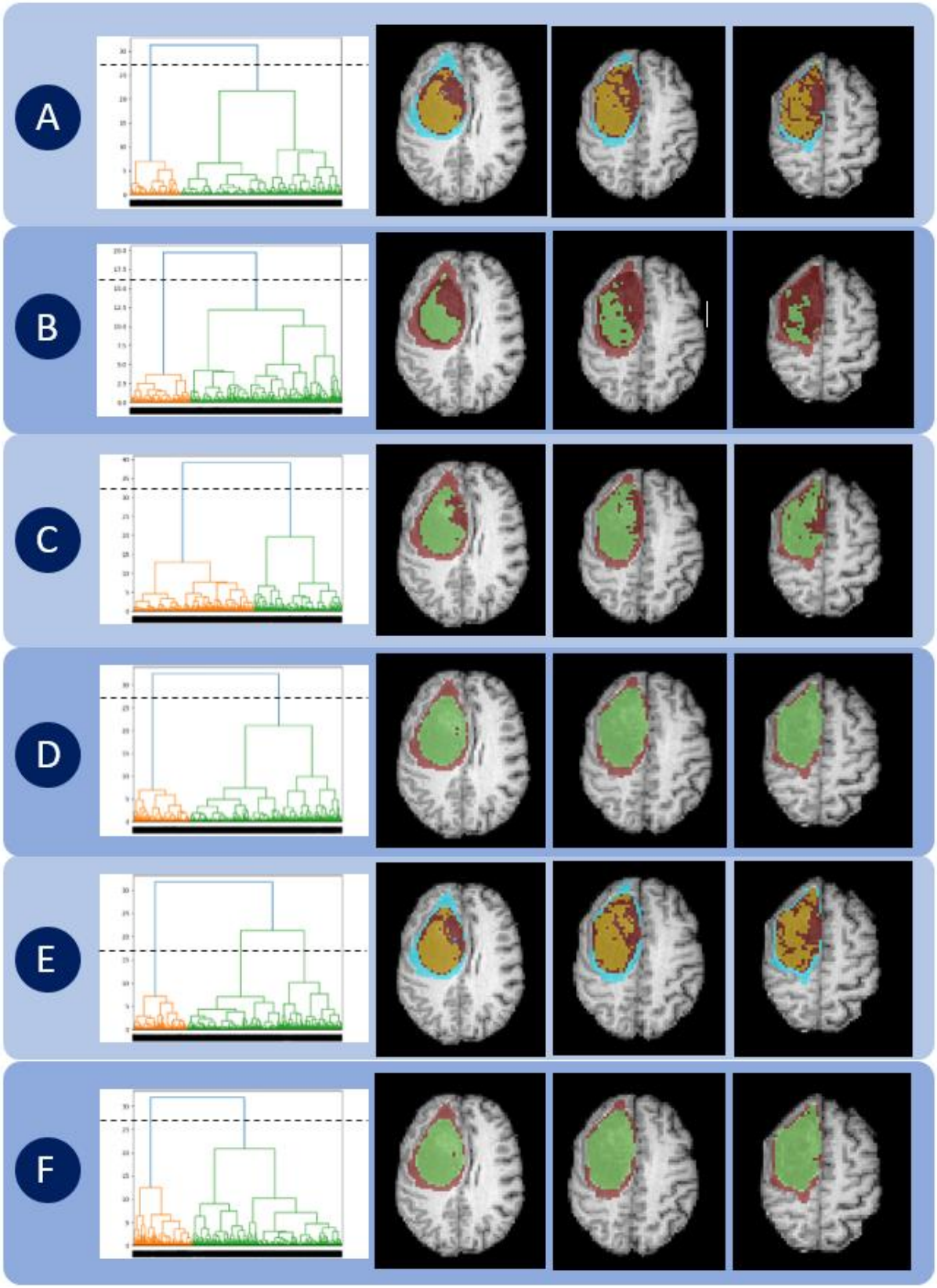

Figure 18: Dendrogram and the location of the clusters in slice 4, 8, and 11 within patient 003 for each clustering method (letters correspond to letters explained in Chapter 3 Methods)

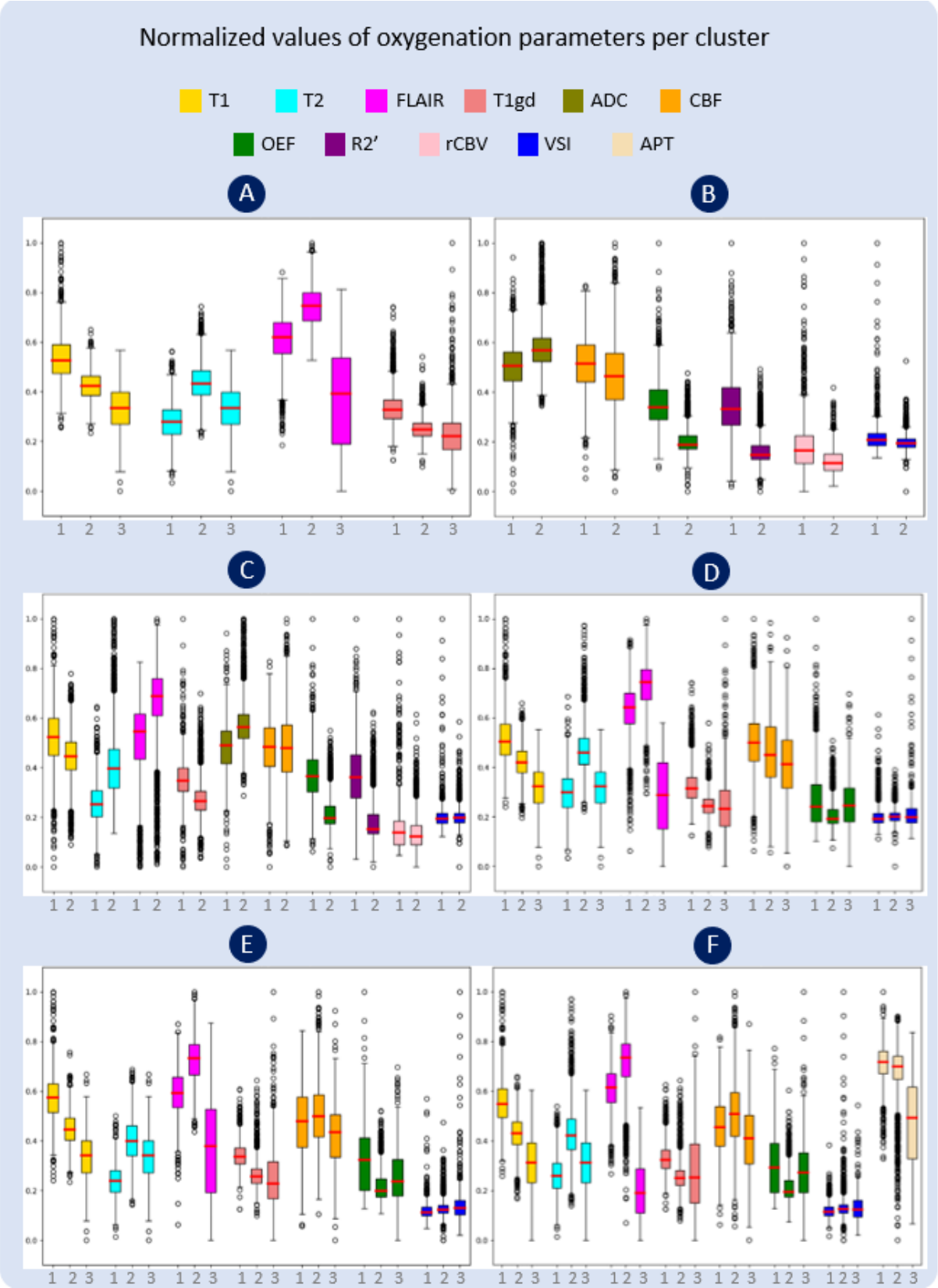

Figure 19 : Box plots of the normalized values of each oxygenation parameter in every cluster for all clustering methods within patient 001.

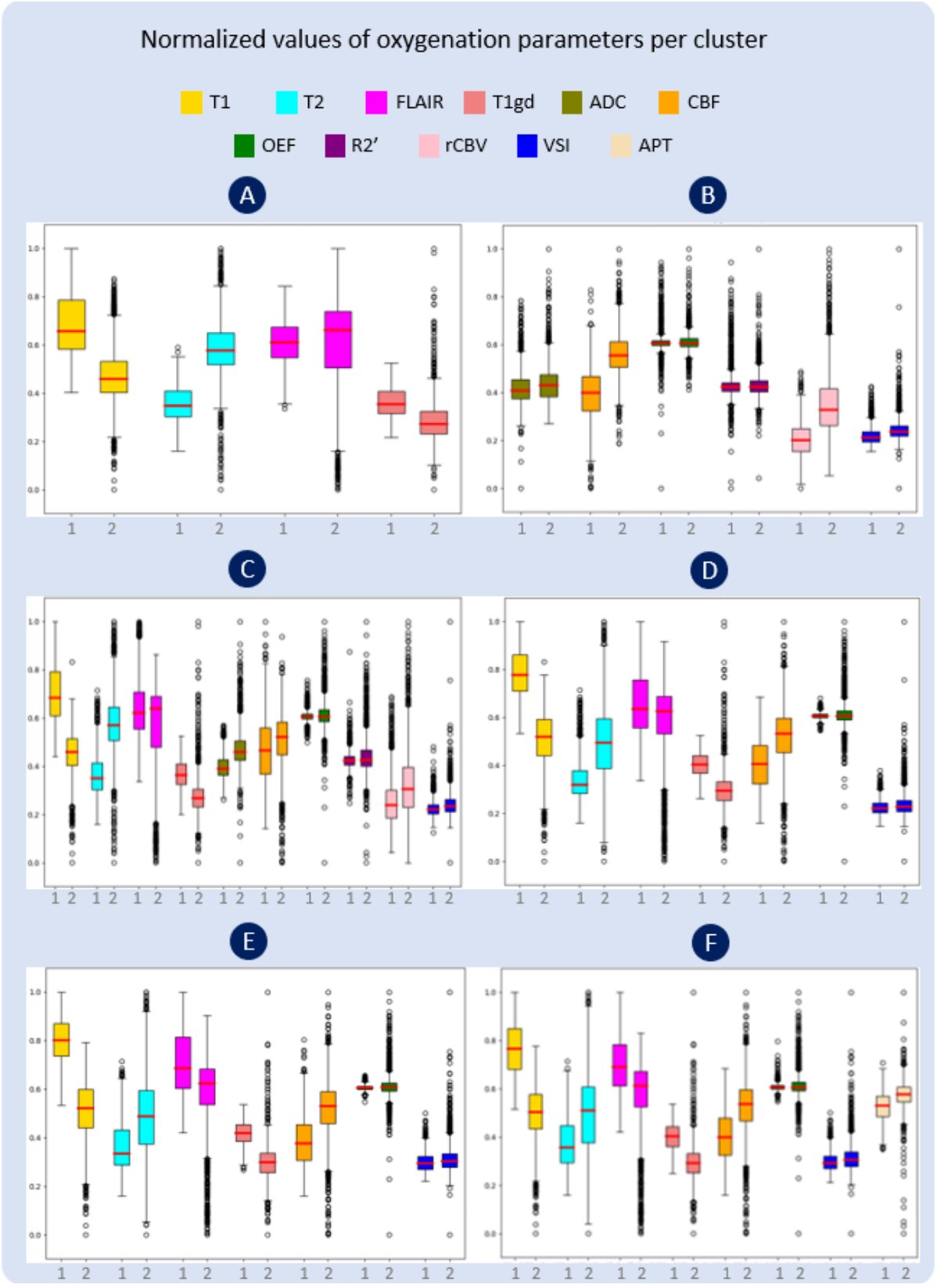

Figure 20: Box plots of the normalized values of each oxygenation parameter in every cluster for all clustering methods within patient 002.

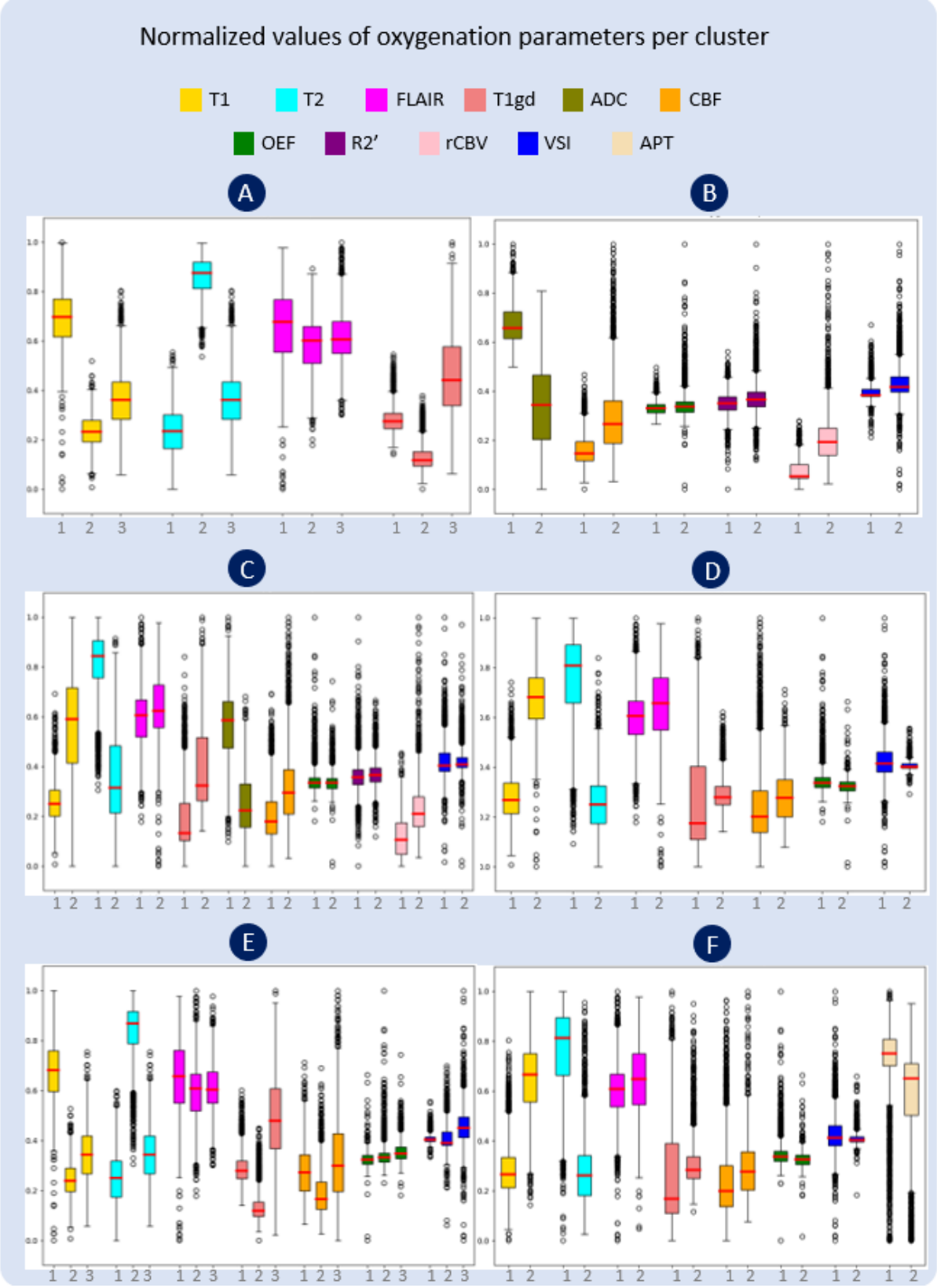

Figure 21: Box plots of the normalized values of each oxygenation parameter in every cluster for all clustering methods within patient 003.

Chapter 5
Discussion

Chapter 5 Discussion

5.1 Interpretation and implications

The present study was designed to create a combined representation of different oxygenation parameters acquired by multiple MRI techniques through using an AI approach. Based on the literature study, hierarchical clustering was chosen as the most suitable approach for this study. The reason for this decision was mainly due to the absence of requiring a priori knowledge and the addition of a dendrogram providing more insight in the clustering process. An additional benefit included the possibility of reducing the algorithms inherent noise sensitivity by tuning input parameters, including distance metrics and linkages.

The optimization of linkage and distance parameters gave expected results, as can be seen in *Table 6*, which shows if the algorithm was able to separate the white matter voxels, gray matter voxels, and cerebrospinal fluid voxels based on the MR images. It can be seen that single linkage results in nearly all data points grouped together, which is not surprising since this linkage method is not very sophisticated as explained in the previous sections. In addition, Average linkage shows its value in distinguishing white matter voxels and gray matter voxels from cerebrospinal fluid voxels, but it is not able to separate the gray matter voxels from the white matter voxels. Based on *Figure 13*, complete linkage and ward linkage shows its capability on clustering three large groups. However, the results in the table show ward linkage and Euclidean distance as the combination with the most accurate clustering results, which is not surprising since these are the most sophisticated distance measures. In *Figure 14* and *Table 7* can be seen that resampling the T1 and FLAIR images to a lower resolution still results in a similar clustering result. Therefore all the clustering in the next parts were done with Ward linkage and Euclidean distance as parameters for the hierarchical clustering.

Since the T1 and FLAIR images with their original resolution resulted in a large number of data points, the running time of the pipeline was long and the required computational power exceeded the available computational power. Therefore we aimed to reduce the computational power needed by compressing the data type used for the data points. However, in *Table 8* can be seen that the duration did not differ extremely and the required memory was exactly the same for different data types. A possible explanation for this might be that T1 and FLAIR maps are generated with intensities as integers. However, for this study solely nifti files of the acquired maps were analysed instead of the original maps. By converting the acquired maps to nifti files, all integers were also converted to floats. So the floats in the T1 and FLAIR maps were actually integers and by compressing these floats into smaller data types, the original integers always stay the same. Thus, the absence of a difference in running time is due this phenomena. However, the duration of the clustering process differs a few minutes. This is probably caused by external factors. Another notable result from *Table 9* is that the clustering result for the data differs if the data points are float16 values. This is an interesting result as it should be exactly the same integers as input data as with float32 and float64 values.

Regarding the tumour clustering, it is interesting to note that in all three patients a more hypoxic core cluster could be detected in the brain tumours, as visualized in *Figure 15, 16, and 17*. This finding was also reported in a similar study of Stadlbauer et al.[26] Another interesting finding is that within patient 001 and patient 003 the number of present clusters differed among the different clustering methods. This can be seen in patient 001 as two clusters are found by using method B and C, while three clusters were found by using method A, D, E, and F. This indicates that a purely data-driven approach might need some prior knowledge on the number of and which different

oxygenation states could be present within a brain tumour. By adding this knowledge in advance, a more targeted search for clusters could be achieved. In the current study, comparing clustering method A with clustering method B in *Figure 19, 20,* and *21* shows that mainly the same regions are coloured. However, method B including solely physiological information shows a core cluster with a slightly different border between the clusters than seen with method A including solely T1, T2, FLAIR, and T1 post-contrast maps. This suggests that advanced MRI shows a process which cannot be detected with conventional MRI.

In *Figure 19* can be seen from the box plots within method B that the two clusters are probably mainly determined by their R2' and OEF value since the boxplots for these parameters have the least overlap when visually comparing cluster 1 with cluster 2. Within method B of patient 002 in *Figure 20* can be seen that the boxplots of CBF and rCBV are the most distinctive parameters for the two cluster found within this patient. This also holds for patient 003 as CBF and rCBV seem to be the most distinctive parameters in combination with the ADC values of these two clusters. These findings, while preliminary, suggest that the clustering pipeline used in this research is able to detect regions with a reduced oxygenation, caused by a reduced OEF or a reduced blood flow and blood volume. In this research, comparing method E with method F shows that adding APT to the other physiological maps does not result in notable different clusters or a different distribution of MR parameters values within the clusters. The result of adding APT to the clustering analysis could be poor due to the already large number of other physiological maps that were included in method E and F. Another possible explanation could be that one or more of the other physiological maps has a similar added value to the clustering result.

5.2 Limitations

Despite the interesting results, this research has some limitations. At first, the number of included patients was very low. This made it harder to draw conclusions on the performance of the clustering pipeline in terms of assessing brain oxygenation. Considering that each patient contains a lot of voxels/data points, there was a lot of data available. However, the voxels originate from only three patients and the result are therefore hard to generalize to patients with other types of brain tumours since the oxygenation in these types could be completely different than the types evaluated in this research.

Another limitation is that not all types of clustering were explored in the literature review. In this research was chosen to only review three well-known clustering methods, while other methods also exist. In addition, each clustering method also has multiple algorithms which use different techniques to cluster the data. For example, Density-based spatial clustering of applications with noise (DBSCAN) is a sophisticated algorithm of density-based clustering. Thus it is hard to compare a clustering method to another clustering method since each method has very simple and very sophisticated algorithms.

Regarding the inclusion of different MR imaging techniques, it is hard to draw conclusions on the importance of the different imaging techniques on the clustering result since some were included in only a few clustering analyses and other techniques were included in other clustering analyses. This makes it hard to compare the different clustering analyses performed in this research and draw a conclusion on the impact of each individual MR imaging technique on the clustering result.

Besides, the clusters were evaluated based on the box plots, showing the distribution of the intensity values within the clusters. However, these values do not have to represent what is happening in the complete physiology of the tumour. Thus a validation of what each cluster truly represents is missing in this research since the clusters are evaluated based on the distribution of data points and not on their correlation with results found in biopsies for example.

5.3 Future research

Further research should be undertaken to investigate the role of clustering in detecting and locating different oxygenation states within brain tumours. To develop a full picture of this process, additional studies will be needed that include a much larger number of patients. When a large number of patients is included, the voxels of all patients can be clustered all at once to find all possible oxygenation scenarios that could potentially be present in brain tumours. Based on these results, a classifier pipeline could be built that clinicians can apply to new patients to detect and locate different oxygenation states. This could play an important role in making treatment decisions.

Besides, other clustering algorithm need to be explored and tested as well. A plethora of clustering algorithms are available and this research only focused on a part of them. A further study comparing different clustering algorithms for clustering image data to identify and locate different oxygenation states within brain tumours is therefore suggested.

In addition, these studies should also have more focus on the impact and value on the clustering result of each individual MRI technique discussed in this research. A future study investigating this by performing the clustering multiple times, but excluding each time one MR image is therefore advised. In addition, the correlation between the results of each MR imaging technique should be investigated since multiple MR imaging techniques could contribute the same information to the clustering analysis. This would generate interesting results on which MR imaging techniques are less important for assessing tumour oxygenation.

Based on the findings in this research, the studies should also implement more knowledge of experienced neuroradiologists regarding brain oxygenation in advance of the clustering instead of the more data-driven approach proposed in this research. The knowledge of experienced neuroradiologists could be used to identify how many different oxygenation states could be expected within specific patients. Using this knowledge as extra input, the clustering result could be improved. However, it should also be investigated if the proposed imaging protocol is feasible to implement in the daily clinical practice.

Instead of focusing on brain oxygenation, further research should be undertaken to investigate the value of clustering in diagnosing brain tumours. By creating these coloured maps, patterns could be unraveled that represent different diagnosis. Stadlbauer et al. already showed that tumour microenvironment mapping showed different phenotypes of brain tumours.[26] By creating a database of these maps combined with the patients diagnosis, treatment plan, and outcomes, new patients could be matched to previous patients in this database. This could also play an important role for the clinicians to decide on the diagnosis and treatment and could therefore potentially improve the survival of these patients, which was eventually the main goal of this research.

Another important issue for future research is to validate the clusters. It could be interesting to investigate if the location of the different clusters also show different results when researching biopsies taken within the same brain tumour. After a patient is scanned and the clustering analysis is performed, biopsies could be taken during resection of the brain tumour. When applying HIF-1 alfa and CD31 staining to the extracted tissue, OEF, CBV, and vessel size values can be evaluated and correlated to the values within the cluster according to the results of the clustering analysis. So instead of finding patterns, validation of the clusters could show what is happening with the physiology in the brain tumour.

5.4 Conclusion

The main goal of the current study was to determine and implement an AI approach to generate a combined representation of multiple oxygenation parameters acquired by different MR imaging techniques. This study has shown that hierarchical clustering is a method which is able to identify and locate different oxygenation states and show the results within a single map. The proposed clustering pipeline in this study could potentially lead to improved diagnosis and survival of patients with brain tumours by locating hypoxic areas within the tumour. Despite the limitations of this study, the proposed pipeline can contribute in unravelling the oxygenation of brain tumours. However, several questions still remain to be unanswered. Further research should focus on comparing different clustering methods, investigating the role of clustering in diagnosis of brain tumours, investigating the value of each individual MR imaging technique on the clustering result, and validating the clusters.

Chapter 6
References

Chapter 6 References

1. Ostrom, Q.T., et al., *CBTRUS statistical report: Primary brain and central nervous system tumors diagnosed in the United States in 2006-2010.* Neuro-oncology, 2013. 15(suppl_2): p. ii1-ii56.
2. Behin, A., et al., *Primary brain tumours in adults.* The Lancet, 2003. 361(9354): p. 323-331.
3. Ostrom, Q.T., et al., *Epidemiology of gliomas.* Cancer Treat Res, 2015. 163: p. 1-14.
4. Newton, H., *Primary brain tumors: review of etiology, diagnosis and treatment.* American family physician, 1994. 49(4): p. 787-797.
5. Louis, D.N., et al., *The 2016 World Health Organization Classification of Tumors of the Central Nervous System: a summary.* Acta Neuropathol, 2016. 131(6): p. 803-20.
6. Reni, M., et al., *Central nervous system gliomas.* Critical Reviews in Oncology/Hematology, 2017. 113: p. 213-234.
7. Vigneswaran, K., S. Neill, and C.G. Hadjipanayis, *Beyond the World Health Organization grading of infiltrating gliomas: advances in the molecular genetics of glioma classification.* Annals of translational medicine, 2015. 3(7).
8. Ohgaki, H., et al., *Genetic pathways to glioblastoma: a population-based study.* Cancer research, 2004. 64(19): p. 6892-6899.
9. Ostrom, Q.T., et al., *CBTRUS Statistical Report: Primary brain and other central nervous system tumors diagnosed in the United States in 2010-2014.* Neuro-oncology, 2017. 19(suppl_5): p. v1-v88.
10. Sant, M., et al., *Survival of European patients with central nervous system tumors.* International journal of cancer, 2012. 131(1): p. 173-185.
11. Davis, M.E. *Epidemiology and overview of gliomas*. in *Seminars in oncology nursing*. 2018. Elsevier.
12. Gray, L.H., et al., *The concentration of oxygen dissolved in tissues at the time of irradiation as a factor in radiotherapy.* The British journal of radiology, 1953. 26(312): p. 638-648.
13. Moulder, J.E. and S. Rockwell, *Tumor hypoxia: its impact on cancer therapy.* Cancer Metastasis Reviews, 1987. 5(4): p. 313-341.
14. Moeller, B.J., R.A. Richardson, and M.W. Dewhirst, *Hypoxia and radiotherapy: opportunities for improved outcomes in cancer treatment.* Cancer Metastasis Reviews, 2007. 26(2): p. 241-248.
15. Moeller, B. and M. Dewhirst, *HIF-1 and tumour radiosensitivity.* British journal of cancer, 2006. 95(1): p. 1-5.
16. Wenzl, T. and J.J. Wilkens, *Theoretical analysis of the dose dependence of the oxygen enhancement ratio and its relevance for clinical applications.* Radiation oncology, 2011. 6(1): p. 1-9.
17. Colliez, F., B. Gallez, and B.F. Jordan, *Assessing tumor oxygenation for predicting outcome in radiation oncology: a review of studies correlating tumor hypoxic status and outcome in the preclinical and clinical settings.* Frontiers in oncology, 2017. 7: p. 10.
18. Spence, A.M., et al., *Regional hypoxia in glioblastoma multiforme quantified with [18F] fluoromisonidazole positron emission tomography before radiotherapy: correlation with time to progression and survival.* Clinical Cancer Research, 2008. 14(9): p. 2623-2630.
19. Chavhan, G.B., et al., *Principles, techniques, and applications of T2*-based MR imaging and its special applications.* J Radiographics, 2009. 29(5): p. 1433-1449.
20. Zhang, J., et al., *Blood-oxygenation-level-dependent-(BOLD-) based R2' MRI study in monkey model of reversible middle cerebral artery occlusion.* 2011. 2011.
21. Dai, W., A. Shankaranarayanan, and D.C. Alsop, *Volumetric measurement of perfusion and arterial transit delay using hadamard encoded continuous arterial spin labeling.* Magnetic resonance in medicine, 2013. 69(4): p. 1014-1022.

22. Stone, A.J. and N.P. Blockley, *A streamlined acquisition for mapping baseline brain oxygenation using quantitative BOLD.* Neuroimage, 2017. 147: p. 79-88.
23. Kellner, E., et al., *MR evaluation of vessel size imaging of human gliomas: Validation by histopathology.* Journal of Magnetic Resonance Imaging, 2015. 42(4): p. 1117-1125.
24. Greenspan, H., B.v. Ginneken, and R.M. Summers, *Guest Editorial Deep Learning in Medical Imaging: Overview and Future Promise of an Exciting New Technique.* IEEE Transactions on Medical Imaging, 2016. 35(5): p. 1153-1159.
25. Shin, H.-C., et al., *Deep convolutional neural networks for computer-aided detection: CNN architectures, dataset characteristics and transfer learning.* IEEE transactions on medical imaging, 2016. 35(5): p. 1285-1298.
26. Stadlbauer, A., et al., *Intratumoral heterogeneity of oxygen metabolism and neovascularization uncovers 2 survival-relevant subgroups of IDH1 wild-type glioblastoma.* Neuro-oncology, 2018. 20(11): p. 1536-1546.
27. Leng, Y., et al., *Radiomics in gliomas: A promising assistance for glioma clinical research.* Zhong Nan Da Xue Xue Bao Yi Xue Ban, 2018. 43(4): p. 354-359.
28. Zhou, T., et al., *Hi-net: hybrid-fusion network for multi-modal MR image synthesis.* IEEE transactions on medical imaging, 2020. 39(9): p. 2772-2781.
29. Dar, S.U., et al., *Image synthesis in multi-contrast MRI with conditional generative adversarial networks.* IEEE transactions on medical imaging, 2019. 38(10): p. 2375-2388.
30. Cho, H.-h. and H. Park. *Classification of low-grade and high-grade glioma using multi-modal image radiomics features*. in *2017 39th Annual International Conference of the IEEE Engineering in Medicine and Biology Society (EMBC)*. 2017. IEEE.
31. Li, Z., et al., *Deep learning based radiomics (DLR) and its usage in noninvasive IDH1 prediction for low grade glioma.* Scientific reports, 2017. 7(1): p. 1-11.
32. White, C.M., et al., *Regional and voxel-wise comparisons of blood flow measurements between dynamic susceptibility contrast magnetic resonance imaging (DSC-MRI) and arterial spin labeling (ASL) in brain tumors.* Journal of Neuroimaging, 2014. 24(1): p. 23-30.
33. Deibler, A., et al., *Arterial spin-labeling in routine clinical practice, part 1: technique and artifacts.* American Journal of Neuroradiology, 2008. 29(7): p. 1228-1234.
34. Wolf, R.L. and J.A. Detre, *Clinical neuroimaging using arterial spin-labeled perfusion magnetic resonance imaging.* Neurotherapeutics, 2007. 4(3): p. 346-359.
35. Warnert, E., et al., *P04. 11 Voxelwise correlation between vascular MRI parameters obtained with ASL and DSC is decreased in IDH-wt non-enhancing glioma.* Neuro-oncology, 2019. 21(Suppl 3): p. iii31.
36. Petcharunpaisan, S., J. Ramalho, and M. Castillo, *Arterial spin labeling in neuroimaging.* World journal of radiology, 2010. 2(10): p. 384.
37. Yun, T.J., et al., *Transit time corrected arterial spin labeling technique aids to overcome delayed transit time effect.* Neuroradiology, 2018. 60(3): p. 255-265.
38. Alsaedi, A., et al., *Overview and Critical Appraisal of Arterial Spin Labelling Technique in Brain Perfusion Imaging.* Contrast media & molecular imaging, 2018. 2018: p. 5360375-5360375.
39. Cohen, A.D., et al., *Longitudinal reproducibility of MR perfusion using 3D pseudocontinuous arterial spin labeling with Hadamard-encoded multiple postlabeling delays.* Journal of Magnetic Resonance Imaging, 2020. 51(6): p. 1846-1853.
40. Günther, M. *Highly efficient accelerated acquisition of perfusion inflow series by cycled arterial spin labeling*. in *Proceedings of the 15th Annual Meeting of ISMRM*. 2007.
41. Dai, W., et al., *Reduced resolution transit delay prescan for quantitative continuous arterial spin labeling perfusion imaging.* Magnetic resonance in medicine, 2012. 67(5): p. 1252-1265.
42. Kiselev, V.G., et al., *Vessel size imaging in humans.* Magnetic Resonance in Medicine: An Official Journal of the International Society for Magnetic Resonance in Medicine, 2005. 53(3): p. 553-563.

43. Shiroishi, M.S., et al., *Principles of T2*-weighted dynamic susceptibility contrast MRI technique in brain tumor imaging.* Journal of Magnetic Resonance Imaging, 2015. 41(2): p. 296-313.
44. Hsu, Y.Y., et al., *Vessel size imaging using dual contrast agent injections.* Journal of Magnetic Resonance Imaging: An Official Journal of the International Society for Magnetic Resonance in Medicine, 2009. 30(5): p. 1078-1084.
45. Boxerman, J.L., et al., *MR contrast due to intravascular magnetic susceptibility perturbations.* Magnetic resonance in medicine, 1995. 34(4): p. 555-566.
46. Beaumont, M., et al., *Characterization of tumor angiogenesis in rat brain using iron-based vessel size index MRI in combination with gadolinium-based dynamic contrast-enhanced MRI.* Journal of Cerebral Blood Flow Metabolism, 2009. 29(10): p. 1714-1726.
47. Valable, S., et al., *Assessment of blood volume, vessel size, and the expression of angiogenic factors in two rat glioma models: a longitudinal in vivo and ex vivo study.* NMR in Biomedicine, 2008. 21(10): p. 1043-1056.
48. Lemasson, B., et al., *In vivo imaging of vessel diameter, size, and density: a comparative study between MRI and histology.* Magnetic resonance in medicine, 2013. 69(1): p. 18-26.
49. Chakhoyan, A., et al., *Validation of vessel size imaging (VSI) in high-grade human gliomas using magnetic resonance imaging, image-guided biopsies, and quantitative immunohistochemistry.* Scientific reports, 2019. 9(1): p. 1-8.
50. Fatterpekar, G.M., et al., *Treatment-related change versus tumor recurrence in high-grade gliomas: a diagnostic conundrum—use of dynamic susceptibility contrast-enhanced (DSC) perfusion MRI.* American Journal of Roentgenology, 2012. 198(1): p. 19-26.
51. Cha, S., *Update on brain tumor imaging: from anatomy to physiology.* American Journal of Neuroradiology, 2006. 27(3): p. 475-487.
52. Knopp, E.A., et al., *Glial neoplasms: dynamic contrast-enhanced T2*-weighted MR imaging.* Radiology, 1999. 211(3): p. 791-798.
53. Law, M., et al., *Comparison of cerebral blood volume and vascular permeability from dynamic susceptibility contrast-enhanced perfusion MR imaging with glioma grade.* American Journal of Neuroradiology, 2004. 25(5): p. 746-755.
54. Bedekar, D., T. Jensen, and K.M. Schmainda, *Standardization of relative cerebral blood volume (rCBV) image maps for ease of both inter-and intrapatient comparisons.* Magnetic resonance in medicine, 2010. 64(3): p. 907-913.
55. Korfiatis, P. and B. Erickson, *The basics of diffusion and perfusion imaging in brain tumors.* Applied radiology, 2014. 43(7): p. 22.
56. Eis, M., T. Els, and M. Hoehn-Berlage, *High resolution quantitative relaxation and diffusion MRI of three different experimental brain tumors in rat.* Magnetic resonance in medicine, 1995. 34(6): p. 835-844.
57. Le Bihan, D., et al., *Separation of diffusion and perfusion in intravoxel incoherent motion MR imaging.* Radiology, 1988. 168(2): p. 497-505.
58. Herneth, A.M., S. Guccione, and M. Bednarski, *Apparent diffusion coefficient: a quantitative parameter for in vivo tumor characterization.* European journal of radiology, 2003. 45(3): p. 208-213.
59. Benveniste, H., L.W. Hedlund, and G.A. Johnson, *Mechanism of detection of acute cerebral ischemia in rats by diffusion-weighted magnetic resonance microscopy.* Stroke, 1992. 23(5): p. 746-754.
60. Bulakbasi, N., et al., *Combination of single-voxel proton MR spectroscopy and apparent diffusion coefficient calculation in the evaluation of common brain tumors.* American Journal of Neuroradiology, 2003. 24(2): p. 225-233.
61. Yamasaki, F., et al., *Apparent diffusion coefficient of human brain tumors at MR imaging.* Radiology, 2005. 235(3): p. 985-991.

62. Hein, P.A., et al., *Diffusion-weighted imaging in the follow-up of treated high-grade gliomas: tumor recurrence versus radiation injury.* American Journal of Neuroradiology, 2004. 25(2): p. 201-209.
63. Lee, W.J., et al., *Diffusion-weighted MR imaging for the differentiation of true progression from pseudoprogression following concomitant radiotherapy with temozolomide in patients with newly diagnosed high-grade gliomas.* Academic radiology, 2012. 19(11): p. 1353-1361.
64. Zeng, Q.-S., et al., *Distinction between recurrent glioma and radiation injury using magnetic resonance spectroscopy in combination with diffusion-weighted imaging.* International Journal of Radiation Oncology Biology Physics, 2007. 68(1): p. 151-158.
65. Yablonskiy, D.A., A.L. Sukstanskii, and X. He, *Blood oxygenation level-dependent (BOLD)-based techniques for the quantification of brain hemodynamic and metabolic properties–theoretical models and experimental approaches.* NMR in Biomedicine, 2013. 26(8): p. 963-986.
66. Ogawa, S., et al., *Brain magnetic resonance imaging with contrast dependent on blood oxygenation.* Proceedings of the National Academy of Sciences, 1990. 87(24): p. 9868-9872.
67. An, H. and W. Lin, *Impact of intravascular signal on quantitative measures of cerebral oxygen extraction and blood volume under normo-and hypercapnic conditions using an asymmetric spin echo approach.* Magnetic Resonance in Medicine: An Official Journal of the International Society for Magnetic Resonance in Medicine, 2003. 50(4): p. 708-716.
68. Hajnal, J.V., et al., *High signal regions in normal white matter shown by heavily T2-weighted CSF nulled IR sequences.* J Comput Assist Tomogr, 1992. 16(4): p. 506-513.
69. Blockley, N.P. and A.J. Stone, *Improving the specificity of R2′ to the deoxyhaemoglobin content of brain tissue: Prospective correction of macroscopic magnetic field gradients.* Neuroimage, 2016. 135: p. 253-260.
70. Wu, B., et al., *An overview of CEST MRI for non-MR physicists.* EJNMMI physics, 2016. 3(1): p. 1-21.
71. Vinogradov, E., A.D. Sherry, and R.E. Lenkinski, *CEST: from basic principles to applications, challenges and opportunities.* Journal of magnetic resonance, 2013. 229: p. 155-172.
72. Kogan, F., H. Hariharan, and R. Reddy, *Chemical exchange saturation transfer (CEST) imaging: description of technique and potential clinical applications.* Current radiology reports, 2013. 1(2): p. 102-114.
73. Van Zijl, P.C. and N.N. Yadav, *Chemical exchange saturation transfer (CEST): what is in a name and what isn't?* Magnetic resonance in medicine, 2011. 65(4): p. 927-948.
74. Qian, Z., et al., *Differentiation of glioblastoma from solitary brain metastases using radiomic machine-learning classifiers.* Cancer Letters, 2019. 451: p. 128-135.
75. Artzi, M., I. Bressler, and D. Ben Bashat, *Differentiation between glioblastoma, brain metastasis and subtypes using radiomics analysis.* Journal of Magnetic Resonance Imaging, 2019. 50(2): p. 519-528.
76. van der Voort, S.R., et al., *Predicting the 1p/19q codeletion status of presumed low-grade glioma with an externally validated machine learning algorithm.* Clinical Cancer Research, 2019. 25(24): p. 7455-7462.
77. Shofty, B., et al., *MRI radiomics analysis of molecular alterations in low-grade gliomas.* International journal of computer assisted radiology surgery, 2018. 13(4): p. 563-571.
78. Zhang, X., et al., *Radiomics strategy for molecular subtype stratification of lower-grade glioma: detecting IDH and TP53 mutations based on multimodal MRI.* Journal of Magnetic Resonance Imaging, 2018. 48(4): p. 916-926.
79. Zhou, H., et al., *Machine learning reveals multimodal MRI patterns predictive of isocitrate dehydrogenase and 1p/19q status in diffuse low-and high-grade gliomas.* Journal of neuro-oncology, 2019. 142(2): p. 299-307.
80. Chang, K., et al., *Residual convolutional neural network for the determination of IDH status in low-and high-grade gliomas from MR imaging.* Clinical Cancer Research, 2018. 24(5): p. 1073-1081.

81. Lu, C.-F., et al., *Machine learning–based radiomics for molecular subtyping of gliomas.* Clinical Cancer Research, 2018. 24(18): p. 4429-4436.
82. Chang, P., et al., *Deep-learning convolutional neural networks accurately classify genetic mutations in gliomas.* American Journal of Neuroradiology, 2018. 39(7): p. 1201-1207.
83. Zhou, H., et al., *MRI features predict survival and molecular markers in diffuse lower-grade gliomas.* Neuro-oncology, 2017. 19(6): p. 862-870.
84. Kickingereder, P., et al., *Radiomic profiling of glioblastoma: identifying an imaging predictor of patient survival with improved performance over established clinical and radiologic risk models.* Radiology, 2016. 280(3): p. 880-889.
85. Prasanna, P., et al., *Radiomic features from the peritumoral brain parenchyma on treatment-naive multi-parametric MR imaging predict long versus short-term survival in glioblastoma multiforme: preliminary findings.* European radiology, 2017. 27(10): p. 4188-4197.
86. Galldiks, N., M. Kocher, and K.-J. Langen, *Pseudoprogression after glioma therapy: an update.* Expert review of neurotherapeutics, 2017. 17(11): p. 1109-1115.
87. Kim, J.Y., et al., *Incorporating diffusion-and perfusion-weighted MRI into a radiomics model improves diagnostic performance for pseudoprogression in glioblastoma patients.* Neuro-oncology, 2019. 21(3): p. 404-414.
88. Hu, X., et al., *Support vector machine multiparametric MRI identification of pseudoprogression from tumor recurrence in patients with resected glioblastoma.* Journal of Magnetic Resonance Imaging, 2011. 33(2): p. 296-305.
89. Jang, B.-S., et al., *Prediction of pseudoprogression versus progression using machine learning algorithm in glioblastoma.* Scientific reports, 2018. 8(1): p. 1-9.
90. Bacchi, S., et al., *Deep learning in the detection of high-grade glioma recurrence using multiple MRI sequences: a pilot study.* Journal of Clinical Neuroscience, 2019. 70: p. 11-13.
91. Akbari, H., et al., *Histopathology-validated machine learning radiographic biomarker for noninvasive discrimination between true progression and pseudo-progression in glioblastoma.* Cancer, 2020. 126(11): p. 2625-2636.
92. Li, M., et al., *DC-AL GAN: pseudoprogression and true tumor progression of glioblastoma multiform image classification based on DCGAN and AlexNet.* Medical physics, 2020. 47(3): p. 1139-1150.
93. Goodfellow, I.J., et al., *Generative adversarial networks.* arXiv preprint arXiv:. 2014.
94. Wolterink, J.M., et al. *Deep MR to CT synthesis using unpaired data*. in *International workshop on simulation and synthesis in medical imaging*. 2017. Springer.
95. Hiasa, Y., et al. *Cross-modality image synthesis from unpaired data using CycleGAN*. in *International workshop on simulation and synthesis in medical imaging*. 2018. Springer.
96. Wolterink, J.M., et al. *MR-to-CT synthesis using cycle-consistent generative adversarial networks*. in *Proc. Neural Inf. Process. Syst.(NIPS)*. 2017.
97. Nie, D., et al., *Medical image synthesis with deep convolutional adversarial networks.* IEEE Transactions on Biomedical Engineering, 2018. 65(12): p. 2720-2730.
98. Chartsias, A., et al. *Adversarial image synthesis for unpaired multi-modal cardiac data*. in *International workshop on simulation and synthesis in medical imaging*. 2017. Springer.
99. Ben-Cohen, A., et al. *Virtual PET images from CT data using deep convolutional networks: initial results*. in *International workshop on simulation and synthesis in medical imaging*. 2017. Springer.
100. Bi, L., et al., *Synthesis of positron emission tomography (PET) images via multi-channel generative adversarial networks (GANs)*, in *Molecular imaging, reconstruction and analysis of moving body organs, and stroke imaging and treatment*. 2017, Springer. p. 43-51.
101. Zhu, J.-Y., et al. *Unpaired image-to-image translation using cycle-consistent adversarial networks*. in *Proceedings of the IEEE international conference on computer vision*. 2017.
102. Ranzato, M.A., et al. *A unified energy-based framework for unsupervised learning*. in *Artificial Intelligence and Statistics*. 2007. PMLR.

103. Sevetlidis, V., M.V. Giuffrida, and S.A. Tsaftaris. *Whole image synthesis using a deep encoder-decoder network*. in *International Workshop on Simulation and Synthesis in Medical Imaging*. 2016. Springer.
104. Huang, H., et al., *Introvae: Introspective variational autoencoders for photographic image synthesis.* arXiv preprint arXiv:.06358, 2018.
105. Costa, P., et al., *End-to-end adversarial retinal image synthesis.* IEEE transactions on medical imaging, 2017. 37(3): p. 781-791.
106. MacQueen, J. *Some methods for classification and analysis of multivariate observations*. in *Proceedings of the fifth Berkeley symposium on mathematical statistics and probability*. 1967. Oakland, CA, USA.
107. Xiong, H., J. Wu, and J. Chen, *K-means clustering versus validation measures: a data-distribution perspective.* IEEE Transactions on Systems, Man, Cybernetics, Part B, 2008. 39(2): p. 318-331.
108. Pena, J.M., J.A. Lozano, and P. Larranaga, *An empirical comparison of four initialization methods for the k-means algorithm.* Pattern recognition letters, 1999. 20(10): p. 1027-1040.
109. Li, A., et al., *Unsupervised analysis of transcriptomic profiles reveals six glioma subtypes.* Cancer research, 2009. 69(5): p. 2091-2099.
110. Network, C.G.A.R., *Comprehensive, integrative genomic analysis of diffuse lower-grade gliomas.* New England Journal of Medicine, 2015. 372(26): p. 2481-2498.
111. Freije, W.A., et al., *Gene expression profiling of gliomas strongly predicts survival.* Cancer research, 2004. 64(18): p. 6503-6510.
112. Young, J.D., C. Cai, and X. Lu, *Unsupervised deep learning reveals prognostically relevant subtypes of glioblastoma.* BMC bioinformatics, 2017. 18(11): p. 5-17.
113. Uppada, S.K., *Centroid based clustering algorithms—A clarion study.* J International Journal of Computer Science

Information Technologies, 2014. 5(6): p. 7309-7313.
114. Kameshwaran, K., K.J.I.J.o.C.S. Malarvizhi, and I. Technologies, *Survey on clustering techniques in data mining.* 2014. 5(2): p. 2272-2276.
115. Peng, R., *Exploratory data analysis with R*. 2012: Lulu. com.
116. Gameti, N.R. and K.J. Sarvakar, *Density Based Methods to Discover Clusters with Arbitrary shape in weka.*
117. Kaufman, L. and P.J. Rousseeuw, *Finding groups in data: an introduction to cluster analysis*. Vol. 344. 2009: John Wiley & Sons.
118. Bergstra, J. and Y. Bengio, *Random search for hyper-parameter optimization.* Journal of machine learning research, 2012. 13(2).
119. Bergstra, J., et al. *Algorithms for hyper-parameter optimization*. in *25th annual conference on neural information processing systems (NIPS 2011)*. 2011. Neural Information Processing Systems Foundation.
120. Hutter, F., H.H. Hoos, and K. Leyton-Brown. *Sequential model-based optimization for general algorithm configuration*. in *International conference on learning and intelligent optimization*. 2011. Springer.
121. Wu, J., et al., *Hyperparameter optimization for machine learning models based on Bayesian optimization.* Journal of Electronic Science, 2019. 17(1): p. 26-40.
122. He, X. and D.A.J.M.R.i.M.A.O.J.o.t.I.S.f.M.R.i.M. Yablonskiy, *Quantitative BOLD: mapping of human cerebral deoxygenated blood volume and oxygen extraction fraction: default state.* 2007. 57(1): p. 115-126.
123. Villanueva-Meyer, J.E., M.C. Mabray, and S.J.N. Cha, *Current clinical brain tumor imaging.* 2017. 81(3): p. 397-415.
124. Yushkevich, P.A., et al., *User-guided 3D active contour segmentation of anatomical structures: significantly improved efficiency and reliability.* 2006. 31(3): p. 1116-1128.

Chapter 7
Appendices

Appendix A

ITEM (Imaging for Tumor Environment Mapping) protocol

Aim: Validation of CEST and Oxygenation MRI maps in human glioma with pathology measurements. This project has been approved by the local ethical review board (MEC-2020-0002). For more details about this project contact:

Esther Warnert, Assistant professor, PI: e.warnert@erasmusmc.nl
Yulun Wu, PhD candidate from Radiology: y.wu@erasmusmc.nl
Fatemehsadat Arzanforoosh, PhD candidate from Radiology: f.arzanforoosh@erasmusmc.nl
Marion Smits, MD, PhD, Professor, Promotor: marion.smits@erasmusmc.nl

Use 32 channel head coil .
It must be in Research Mode

Scan sequence	To obtain	Duration
Loc	Knowing where the brain is	00:17
Asset	Allows for acceleration of other scans	00:05
T1 pre-contrast	Structure, needed to check enhancing regions after injection	03:02
T2w FLAIR	Structure, identification of hyperintense regions	04:21
DWI Multi B-value	Allows for intravoxel inchorent motion analysis (IVIM). Gives apparent diffusion coefficient and allows for perfusion fraction estimates.	04:25
DWI two b-value	Needed to optimize IVIM analysis	00:40
DTI	Tractography for SAFE trial	03:50
eASL	Non-invasive perfusion measurements and transit time assessments	05:22
CEST_spec1	Chemical exchange saturation transfer imaging to asses amide proton transfer weighted imaging (APT)	04:40
CEST_spec2		04:40
B1 map	Needed to optimize CEST analysis	00:28
FASE imaging block	Asymmetric spin echo sequence, allows for assessment of local oxygenation	07:20
Contrabolus 7.5 cc met 7.5cc/s + 15 cc NaCl 5 cc/s		
T2 propeller	Structure, required for navigation?	01:50
T1 post contrast	Structure, sssessing enhancement	03:02
HEPI multiphase	Will give rCBV/rCBF/Vessel architecture measurements. Run while injecting second bolus: **Contrabolus 7.5 cc met 7.5cc/s + 15 cc NaCl 5 cc/s**	03:03
Hepi scans	Needed for optimization of hepi analysis	00:26

Appendix B

Python script for clustering image data with ward linkage and Euclidean distance:

```
import numpy as numpy
import nibabel as nib
import os
import pandas as pd
import numpy as np

import scipy.cluster.hierarchy as shc
import matplotlib.pyplot as plt
import matplotlib

from sklearn.cluster import AgglomerativeClustering


# loading data
path_ADC = "/scratch/mrosbergen/maps/ADC_t1gd.nii.gz"
path_CBF = "/scratch/mrosbergen/maps/CBF_t1gd.nii.gz"
path_DBV = "/scratch/mrosbergen/maps/DBV_t1gd.nii.gz"
path_eASL = "/scratch/mrosbergen/maps/eASL_0_t1gd.nii.gz"
path_HEPI = "/scratch/mrosbergen/maps/HEPI_0_t1gd.nii.gz"
path_R2 = "/scratch/mrosbergen/maps/R2p_t1gd.nii.gz"
path_rCBV = "/scratch/mrosbergen/maps/rCBV_t1gd.nii.gz"
path_VSI = "/scratch/mrosbergen/maps/VSI_t1gd.nii.gz"

path_flair = "/scratch/mrosbergen/maps/flair.nii.gz"
path_t2 = "/scratch/mrosbergen/maps/t2.nii.gz"
path_t1 = "/scratch/mrosbergen/maps/t1.nii.gz"
path_t1gd = "/scratch/mrosbergen/maps/t1gd.nii.gz"

path_tmask = "/scratch/mrosbergen/maps/Tumor.nii.gz"
path_gm = "/scratch/mrosbergen/maps/t1_gm_mask.nii.gz"
path_wm = "/scratch/mrosbergen/maps/t1_wm_mask.nii.gz"
path_csf = "/scratch/mrosbergen/maps/t1_csf_mask.nii.gz"

img_flair = nib.load(path_flair)

img_t2 = nib.load(path_t2)

img_t1 = nib.load(path_t1)

img_t1gd = nib.load(path_t1gd)



# loading mask and setting all values above 0 to 1
img_tmask = nib.load(path_tmask)
```

```
tmask = img_tmask.get_fdata()
tmask[tmask>0] = 1 # two difference mask values greater than 0 set both to 1

img_gm = nib.load(path_gm)
mask_gm = img_gm.get_fdata()

img_wm = nib.load(path_wm)
mask_wm = img_wm.get_fdata()

img_csf = nib.load(path_csf)
mask_csf = img_csf.get_fdata()




# change image data into numpy data
t11 = img_t1.get_fdata()
flair1 = img_flair.get_fdata()
t21 = img_t2.get_fdata()




# multiply tumour mask with all volumes maps
t1_t = tmask*t11
flair_t = tmask*flair1
t2_t = tmask*t21

# multiply grey matter mask with all volumes maps
t1_gm = mask_gm*t11
flair_gm = mask_gm*flair1
t2_gm = mask_gm*t21

# multiply white matter mask with all volumes maps
t1_wm = mask_wm*t11
flair_wm = mask_wm*flair1
t2_wm = mask_wm*t21

# multiply csf mask with all volumes maps
t1_csf = mask_csf*t11
flair_csf = mask_csf*flair1
t2_csf = mask_csf*t21




gm_v = []
```

```
gm_coordinates = []

for vy in range(t11.shape[0]):
    for vx in range(t11.shape[1]):
        for vz in range(t11.shape[2]):

            if t1_gm[vy, vx, vz] != 0:
                combi = [t1_gm[vy, vx, vz], flair_gm[vy, vx, vz]]
                gm_v.append(combi)
                gm_coordinates.append([[vy], [vx], [vz]])
            if len(gm_v) == 80000:
                break

gm_v = np.array(gm_v)
gm_coordinates = np.array(gm_coordinates)

gm_v = (gm_v - np.min(gm_v)) / ( np.max(gm_v) - np.min(gm_v))

wm_v = []
wm_coordinates =[]

for vy in range(t11.shape[0]):
    for vx in range(t11.shape[1]):
        for vz in range(t11.shape[2]):

            if t1_wm[vy, vx, vz] != 0:
                combi = [t1_wm[vy, vx, vz], flair_wm[vy, vx, vz]]
                wm_v.append(combi)
                wm_coordinates.append([[vy], [vx], [vz]])
            if len(wm_v) == 80000:
                break

wm_v = np.array(wm_v)
wm_coordinates = np.array(wm_coordinates)

wm_v = (wm_v - np.min(wm_v)) / ( np.max(wm_v) - np.min(wm_v))

csf_v = []
csf_coordinates = []

for vy in range(t11.shape[0]):
    for vx in range(t11.shape[1]):
        for vz in range(t11.shape[2]):

            if t1_csf[vy, vx, vz] != 0:
                combi = [t1_csf[vy, vx, vz], flair_csf[vy, vx, vz]]
                csf_v.append(combi)
                csf_coordinates.append([[vy], [vx], [vz]])
            if len(csf_v) == 80000:
```

```
                break

csf_v = np.array(csf_v)
csf_coordinates = np.array(csf_coordinates)

csf_v = (csf_v - np.min(csf_v)) / ( np.max(csf_v) - np.min(csf_v))

voxels2 = np.concatenate((wm_v,csf_v))
voxels = np.concatenate((gm_v,voxels2))

coordinates2 = np.concatenate((wm_coordinates, csf_coordinates))
coordinates = np.concatenate((gm_coordinates, coordinates2))

matplotlib.use('Agg')




#perform clustering based on dendrogram
cluster = AgglomerativeClustering(n_clusters=3, affinity='euclidean', linkage=
'ward')
labels = cluster.fit_predict(voxels)




#transform labels 1D array into 2D matrix
q=[]
for i in range(len(labels)):
    q.append(labels[i])

q = np.array(q)
q[q == 0] = 3

co=[]
for i in range(len(labels)):
    co.append(coordinates[i,:])
co = np.array(co)




#create array same size as MR images, including labels, all other voxels set t
o 0
img_t1_copy = img_t1.get_fdata()
label_overlay = np.zeros((img_t1_copy.shape[0], img_t1_copy.shape[1], img_t1_c
opy.shape[2]))
```

```
for c in range(co.shape[0]):
    label_overlay[co[c,0], co[c,1], co[c,2]] = q[c]

img = nib.Nifti1Image(label_overlay, np.eye(4))  # Save axis for data (just id
entity)
img.header.get_xyzt_units()
img.to_filename(os.path.join('labels__exp_wmgmcsf_eu_ward_norm.nii.gz'))  # Sa
ve as NiBabel file

img = nib.Nifti1Image(img_t1_copy, np.eye(4))  # Save axis for data (just iden
tity)
img.header.get_xyzt_units()
img.to_filename(os.path.join('t1__exp_wmgmcsf_eu_ward_norm.nii.gz'))  # Save a
s NiBabel file



#results analysis
c1 = len(q[q == 1])
# print('Size cluster 1: ' + str(c1))
c2 = len(q[q == 2])
# print('Size cluster 2: ' + str(c2))
c3 = len(q[q == 3])
# print('Size cluster 3: ' + str(c3))
f = open("results__exp_wmgmcsf_eu_ward_norm.txt", "w")
f.write("Size cluster 1: " + str(c1))
f.write("\nSize cluster 2: " + str(c2))
f.write("\nSize cluster 3: " + str(c3))

c1_gm = []
c1_wm = []
c1_csf = []
c2_gm = []
c2_wm = []
c2_csf = []
c3_gm = []
c3_wm = []
c3_csf = []

co = np.squeeze(co)

for c in range(len(q)):
    if q[c] == 1:
        if mask_gm[co[c,0],co[c,1],co[c,2]] != 0:
            c1_gm.append(q[c])
        if mask_wm[co[c,0],co[c,1],co[c,2]] != 0:
            c1_wm.append(q[c])
```

```
        if mask_csf[co[c,0],co[c,1],co[c,2]] != 0:
            c1_csf.append(q[c])
    if q[c] == 2:
        if mask_gm[co[c,0],co[c,1],co[c,2]] != 0:
            c2_gm.append(q[c])
        if mask_wm[co[c,0],co[c,1],co[c,2]] != 0:
            c2_wm.append(q[c])
        if mask_csf[co[c,0],co[c,1],co[c,2]] != 0:
            c2_csf.append(q[c])
    if q[c] == 3:
        if mask_gm[co[c,0],co[c,1],co[c,2]] != 0:
            c3_gm.append(q[c])
        if mask_wm[co[c,0],co[c,1],co[c,2]] != 0:
            c3_wm.append(q[c])
        if mask_csf[co[c,0],co[c,1],co[c,2]] != 0:
            c3_csf.append(q[c])

f.write("\nNumber gray matter voxels in cluster 1: " + str(len(c1_gm)))
f.write("\nNumber white matter voxels in cluster 1: " + str(len(c1_wm)))
f.write("\nNumber csf voxels in cluster 1: " + str(len(c1_csf)))
f.write("\nNumber gray matter voxels in cluster 2: " + str(len(c2_gm)))
f.write("\nNumber white matter voxels in cluster 2: " + str(len(c2_wm)))
f.write("\nNumber csf voxels in cluster 2: " + str(len(c2_csf)))
f.write("\nNumber gray matter voxels in cluster 3: " + str(len(c3_gm)))
f.write("\nNumber white matter voxels in cluster 3: " + str(len(c3_wm)))
f.write("\nNumber csf voxels in cluster 3: " + str(len(c3_csf)))
f.close()




#3D scatter plot
plt.figure(figsize=(10, 7))
plt.scatter(voxels[:,0], voxels[:,1], c=cluster.labels_, cmap='rainbow')
plt.savefig('scatter__exp_wmgmcsf_eu_ward_norm')
```

Appendix C

Python script to create a dendrogram based on clustering image data with ward linkage and Euclidean distance:

```
import numpy as numpy
import nibabel as nib
import os
import pandas as pd
import numpy as np

import scipy.cluster.hierarchy as shc
import matplotlib.pyplot as plt
import matplotlib

from sklearn.cluster import AgglomerativeClustering


# loading data
path_ADC = "maps_resample_P01/ADC_t1gd_elastix.nii.gz"
path_CBF = "maps_resample_P01/CBF_brain_t1gd_elastix.nii.gz"
path_OEF = "maps_resample_P01/OEF_t1gd_elastix.nii.gz"
path_R2p = "maps_resample_P01/R2p_t1gd_elastix.nii.gz"
path_rCBV = "maps_resample_P01/rCBV_BSW_t1gd_elastix.nii.gz"
path_VSI = "maps_resample_P01/VSI_BSW_t1gd_elastix.nii.gz"
path_APT = "maps_resample_P01/APT P01.nii.gz"

path_flair = "maps_resample_P01/flair_brain_resample.nii.gz"
path_t2 = "maps_resample_P01/t2_brain_resample.nii.gz"
path_t1 = "maps_resample_P01/t1_brain_resample.nii.gz"
path_t1gd = "maps_resample_P01/t1gd_brain_resample.nii.gz"

path_tmask = "maps_resample_P01/Tumour_mask_resampled_p1.nii.gz"

img_ADC = nib.load(path_ADC)
print("shape ADC:")
print(img_ADC.shape)

img_CBF = nib.load(path_CBF)
print("shape CBF:")
print(img_CBF.shape)

img_OEF = nib.load(path_OEF)
print("shape OEF:")
print(img_OEF.shape)

img_R2p = nib.load(path_R2p)
print("shape R2p:")
print(img_R2p.shape)
```

```
img_rCBV = nib.load(path_rCBV)
print("shape rCBV:")
print(img_rCBV.shape)

img_VSI = nib.load(path_VSI)
print("shape VSI:")
print(img_VSI.shape)

img_APT = nib.load(path_APT)
print("shape APT:")
print(img_APT.shape)


img_flair = nib.load(path_flair)
print("shape flair:")
print(img_flair.shape)

img_t2 = nib.load(path_t2)
print("shape t2:")
print(img_t2.shape)

img_t1 = nib.load(path_t1)
print("shape t1:")
print(img_t1.shape)

img_t1gd = nib.load(path_t1gd)
print("shape t1gd:")
print(img_t1gd.shape)



# loading mask and setting all values above 0 to 1
img_tmask = nib.load(path_tmask)
print("shape tumour mask:")
print(img_tmask.shape)
tmask = img_tmask.get_fdata()



# change image data into numpy data
t11 = img_t1.get_fdata()
flair1 = img_flair.get_fdata()
t21 = img_t2.get_fdata()
t1gd1 = img_t1gd.get_fdata()

print(t11.dtype)
print(flair1.dtype)
print(t21.dtype)
```

```
print(t1gd1.dtype)

adc1 = img_ADC.get_fdata()
cbf1 = img_CBF.get_fdata()
oef1 = img_OEF.get_fdata()
r2p1 = img_R2p.get_fdata()
rcbv1 = img_rCBV.get_fdata()
vsi1 = img_VSI.get_fdata()

print(adc1.dtype)
print(cbf1.dtype)
print(oef1.dtype)
print(r2p1.dtype)
print(rcbv1.dtype)
print(vsi1.dtype)



# multiply tumour mask with all volumes maps
t1_t = tmask*t11
flair_t = tmask*flair1
t2_t = tmask*t21
t1gd_t = tmask*t1gd1

adc_t = tmask*adc1
cbf_t = tmask*cbf1
oef_t = tmask*oef1
r2p_t = tmask*r2p1
rcbv_t = tmask*rcbv1
vsi_t = tmask*vsi1




t=[]
t_coordinates=[]


for vy in range(t11.shape[0]):
    for vx in range(t11.shape[1]):
        for vz in range(t11.shape[2]):

            if tmask[vy, vx, vz] != 0:
                combi = [t1_t[vy, vx, vz], t2_t[vy, vx, vz], flair_t[vy, vx, v
z], t1gd_t[vy, vx, vz]]
                t.append(combi)
                t_coordinates.append([[vy], [vx], [vz]])

t = np.array(t)
```

```
t_coordinates = np.array(t_coordinates)



# normalizing values per mri technique
t_t1_norm = t[:,0]
t_t2_norm = t[:,1]
t_flair_norm = t[:,2]
t_t1gd_norm = t[:,3]

t_t1_norm = (t_t1_norm - np.min(t_t1_norm))/(np.max(t_t1_norm) - min(t_t1_norm
))
t_t2_norm = (t_t2_norm - np.min(t_t2_norm))/(np.max(t_t2_norm) - min(t_t2_norm
))
t_flair_norm = (t_flair_norm - np.min(t_flair_norm))/(np.max(t_flair_norm) - m
in(t_flair_norm))
t_t1gd_norm = (t_t1gd_norm - np.min(t_t1gd_norm))/(np.max(t_t1gd_norm) - min(t
_t1gd_norm))

t_norm = [t_t1_norm, t_t2_norm, t_flair_norm, t_t1gd_norm]

t_norm = np.array(t_norm)
t_norm = np.transpose(t_norm)
print(t_norm.shape)



#plot dendogram
matplotlib.use('Agg')
plt.figure()
plt.title("Voxels Dendrogram")
dend = shc.dendrogram(shc.linkage(t_norm, method='ward'))
plt.savefig('dendrogram_exp_tumour_p1_norm_str.png')
```